1   **Thrusts control the thermal maturity of accreted sediments.**

2   Utsav Mannu[1,5*], David Fernández-Blanco[2], Ayumu Miyakawa[3], Taras Gerya[4], and Masataka Kinoshita[5]

3   [1]Discipline of Earth Sciences, Indian Institute of Technology, Gandhinagar 382355, India;

4   [2] Barcelona Center for Subsurface Imaging, Passeig Marítim de Barceloneta 37-49, Barcelona Spain

5   [3] Geological Survey of Japan, AIST, Central 7, Higashi 1-1-1, Tsukuba, Ibaraki, 305-8567, Japan

6   [4]Institute of Geophysics, Department of Earth Sciences, ETH Zurich, Sonneggstrasse, 5, 8092 Zurich, Switzerland

7   [5]Earthquake Research Institute, The University of Tokyo, 1-1-1 Yayoi Bunkyo-ku, Tokyo, 113-0032, Japan

8   *Correspondence to*: Utsav Mannu (utsav.mannu@iitgn.ac.in)

9

10

11

12

13

14

15

16

17

18

19

Abstract.

Thermal maturity assessments of hydrocarbon-generation potential and thermal history rarely consider how upper-plate structures developing during subduction influence the trajectories of accreted sediments. Our thermomechanical models of subduction support that thrusts evolving under variable sedimentation rates and décollement strengths fundamentally influence the trajectory, temperature, and thermal maturity of accreting sediments. This is notably true for the frontal thrust, which pervasively partitions sediments along a low and a high maturity path. Our findings imply that interpretations of the distribution of thermal maturity cannot be detached from accounts of the length and frequency of thrusts and their controlling factors. Our approach takes these factors into consideration and provides a robust uncertainty estimate in maximum exposure temperatures as a function of vitrinite reflectance and burial depth. As a result, our models reduce former inconsistencies between predicted and factual thermal maturity distributions in accretionary wedges.

31

32

33

34

35

36

37

38

39

40

41

42

43

1. Introduction

Organic material transforms into coal, oil, and gas at rates primarily controlled by temperature. This transformation, critical for the hydrocarbon industry, is also useful to study the tectonic and sedimentary evolution of basins and orogens. The extent of this transformation in sediments, known as thermal maturity, can be measured as vitrinite reflectance, i.e., the percentage of incident light reflected from the surface of vitrinite particles in those sediments. Thermal maturity has been used to estimate the thermal evolution of igneous intrusions and seismic slip, the extent of low-grade metamorphism, porosity, and compaction in basin sediments, and the geothermal history of accreting material during subduction (e.g., Bostick and Pawlewicz, 1984; Rabinowitz et al., 2020; Fukuchi et al., 2017; Kamiya et al. 2017).

Inferences on the geothermal history of subduction margins based on thermal maturity depend on the trajectory followed by the accreting sediments (Miyakawa et al., 2019). Low-temperature, high-pressure metamorphic rocks in the subduction wedge are often attributed to the pressure maxima that typically predate the temperature maxima in accreted sediments undergoing diagenesis in the wedge (van Gool and Cawood, 1994). However, the existence of complicated patterns in sediment trajectories is supported by numerical models and field observations (Giunchi & Ricard, 1999). As the orogenic wedge evolves, sediments accreting along different paths reach different depths and velocities and are exposed to different regional peak temperatures. Miyakawa et al. (2019) proposed to subdivide these trajectories based on their final characteristics, like thermal maturity. In this manner, the spatiotemporal evolution of sediments and their thermal maturity is regulated to a first order by the partition of incoming sediments along two endmember pathways; (I) a deeper path leading to elevated thermal maturities and constituted by underthrusted material, the ***high thermal-maturity path***, and (II) a shallower path that

64 typically lies closer to the surface or gets frequently exhumed to near-surface levels, the ***low thermal-maturity***

65 ***path.***

66   Previous studies have used numerical and analogue approaches to study the trajectories of sedimentary

67 particles, and their spatial and pressure-temperature evolution, as a function of changes in erosion, sedimentation,

68 or décollement strength. The trajectory followed by underthrusted sedimentary units is primarily determined by

69 orogenic wedge dynamics and its controlling forces (Plat, 1986). Although these sediments may only be exhumed

70 near the backstop of the wedge, the trajectories of other accreted sediments generally deflect toward the surface

71 under the influence of erosion (Konstantinovskaia and Malavieille, 2005). In fact, sedimentary particle trajectories

72 gradually shift from deflection toward the surface near the front of accretion to final exhumation near the wedge

73 backstop (Wenk and Huhn, 2013). Still, even under-thrusted sediments, which would co-relate to high-maturity

74 paths in our study, have variable pressure-temperature paths (Ruh, 2020). It is important to highlight that the

75 majority of past studies have explored a snapshot of sediment trajectories, assuming that the general nature of

76 trajectories remains relatively fixed with time or is stationary in nature. However, the intrinsic connection between

77 thermal maturity and the comprehensive thermal exposure along the entire trajectory necessitates an in-depth

78 investigation into the dynamic and transitory nature of sediment trajectories.

79   Although there is general consensus on the rate and extent of sediment trajectory transition from horizontal

80 to vertical during accretion, the dynamic perturbations in sediment dynamics have yet to be adequately examined.

81 For instance, while most studies show a great degree of correlation between the initial depth of incoming sediments

82 and their final position in the wedge (e.g., Mulugeta and Koyi, 1992; Willett, 1992), a dynamic fluctuation in this

83 correlation due to thrusting can result in non-stationary exhumation paths for accreting sediments in a wedge (e.g.,

84 Konstantinovskaia and Malavieille, 2005; Miyakawa et al., 2019). Much remains to be explored regarding the

85 partition of high and low thermal maturity paths and how sediments travel inside natural wedges, given the

86 conventional assumption that accreting sediments remain at the same relative depth and translate along the adjacent

87 "layers" without vertical mixing throughout the tectonic evolution of the wedge (Hori and Sakaguchi, 2011).

88   Our assessment identifies a primary gap in existing research: the prediction and mapping of the initial

89 sediment influx to their location in the orogenic wedge. More specifically, the challenge lies in determining which

90 portions of incoming sediment will predominantly constitute the core of the wedge and which will reside at

91 comparatively shallower depths. Given that the maximum exposure temperature estimation from the thermal

92 maturity is inherently reliant on the path of sediments inside the wedge, information on path diversity would

93 inherently constrain the uncertainty in maximum exposure temperature used for the identification of paleothermal

94 structures of subduction zones. Moreover, to better understand the time-depth paths of wedge sediments, their

95 dependence on the initial state of undeformed sediments, and thus their thermal maturity, the factors that control

96 the evolution of subduction-accretion systems, like sedimentation, erosion, and décollement strength, ought to be

97 considered (Mannu et al., 2016; Simpson, 2010).

98   Here, we explore in detail the impact of accretion in a subduction wedge has on the thermal maturity of its

99 sediments. We simulate subduction-accretion using 2D finite-difference thermomechanical models incorporating

100 empirical thermal conductivity values from the Nankai accretionary margin. We track the evolution of thermal

101 maturity by computing vitrinite reflectance ($\%R_o$) on each marker and throughout the model, using three well-

102 established methods of $\%R_o$ computation, as accretion develops the wedge under different sedimentation rates and

103 décollement strengths. These factors notably alter the trajectories and thermal maturities of incoming sediments.

104 Particularly, thrusts define sharp thermal maturity boundaries leading to stark differences in the thermal maturity

105 of sediments that accrete in different thrust blocks, even when they follow similar trajectories and lay nearby.

2. Geological settings and model generalization

We use a generalized model for the subduction of an oceanic plate under a continental plate, with explicit integration of key parameters from the Nankai subduction margin off the Kii island in southwest Japan. The Nankai subduction margin is a product of the ongoing, northwest-directed subduction of the Philippine Sea Plate beneath the Amurian Plate at a convergence rate of 4.1-6.5 cm/yr (Seno et al., 1993; Miyazaki and Heki, 2001; DeMets et al., 2010). Past studies posit the initiation of this subduction within the Nankai region at circa 6 Ma (Kimura et al., 2014). The accretionary wedge adjacent to the Nankai margin is marked by the accretion of thick sediment layers (>1 km), predominantly formed by overlying younger trench sediments atop Shikoku Basin sediments. Mean sedimentation rates of ~0.4 mm/yr for this area are calculated from sediment data onland and may largely reach the trench through submarine channels (Korup et al., 2014).

Another reason to select the Nankai subduction margin is that is it a particularly well-studied accretionary margin regarding its paleo-thermal history and thermal maturity distribution. For example, Underwood et al. (1993) and Sakaguchi (1999) used thermal maturity estimates from Shimanto accretionary wedge in the Nankai subduction margin to suggest that ridge subduction can explain the resulting paleo-heat flow. Following this, Ohmori (1997) published a distribution of thermal maturity and maximum exposure temperature for the Shimanto accretionary wedge identifying out-of-sequence thrusting in the region. The accretionary wedge adjacent to the Kumano forearc basin in the Nankai subduction margin has also been the subject of the NanTroSEIZE (Nankai Trough Seismogenic Zone) project, which drilled C0002 borehole during the 2012 Integrated Ocean Discovery Program Expedition 338. C0002 borehole is located approximately km southwest of Japan's Kii Peninsula in the Kumano Basin, within the Nankai accretionary margin, and extends 3,348 meters below the seafloor. Having data on both thermal maturity and thermal conductivity from the same borehole in subduction wedges is quite uncommon. To our knowledge, the C0002 borehole, located next to the Kumano forearc basin, is the only place where such data can be found in an

128 accretionary wedge. Because of this unique characteristic, the C0002 borehole serves as an excellent dataset for

129 validation purposes. We modify the thermal conductivity computation for sediments and décollement (see Table

130 1) to match the empirical relationship between depth and thermal conductivity, as measured on core samples in the

131 borehole C0002 (Sugihara et al., 2014).

132 While these adjustments render our models somewhat specific to the Nankai accretionary wedge, we propose that

133 the thermal conductivity values and trend are representative of patterns typically observed in forearc basins and

134 accretionary wedges across the globe, making it broadly applicable to general subduction margins. For instance, in

135 our simulations, the sediment thermal conductivity within our wedge steadily increases with depth from 0.96-4.0

136 $Wm^{-1}K^{-1}$, which is within the range of thermal conductivity estimates for comparable depth in other subduction

137 zones, such as the Hikurangi subduction margin, Japan Trench, and Taiwan subduction zone (Fig. S1, Henrys et

138 al. 2003, Lin et al. 2014, Chi and Reed, 2008). As a result, we compare our simulation results not only to thermal

139 maturity values in the Nankai accretionary margin but also to those of the Miura-Boso plate subduction margin in

140 central Japan and the fold and thrust belts of the Western Foothills complex in western Taiwan.

141 **3. Methods**

142 We employ I2VIS, a conservative finite-difference 2-D thermomechanical subduction-accretion model with visco-

143 plastic/brittle rheology (Gerya and Yuen, 2003a, 2003b). The code solves the governing equations for the

144 conservation of mass, momentum, and heat as well as the advection equation with a non-diffusive marker-in-cell

145 scheme constrained by thermal conductivity values inferred from Nankai accretionary wedge. Our numerical

146 approach has several advantages over earlier attempts to simulate thermal maturity in an accretionary wedge, such

147 as a more realistic geothermal profile, variable particle paths, and thermal evolution. In the following sections, we

148 provide information regarding the governing equations, the modified thermal conductivity formulations based on

149 the C0002 borehole, boundary conditions, the rheological model, model setup, surface processes, and the

150 computation of thermal maturity.

3.1 Governing equations

152 The mass conservation is described by the continuity equation with the Boussinesq approximation of

153 incompressibility.

154
$$\frac{\partial v_x}{\partial x} + \frac{\partial v_y}{\partial y} = 0 \qquad (eq.\,1)$$

155 Where v_x and v_y are horizontal and vertical components of velocity.

156 The equation for conservation of momentum with an incompressibility assumption is expressed in the 2D- Stokes

157 equation, for the *x*-axis and *y*-axis, respectively,

158
$$\frac{\partial \sigma_{xx}}{\partial x} + \frac{\partial \sigma_{xy}}{\partial y} = \frac{\partial P}{\partial x} \qquad (eq.\,2)$$

159 where σ_{xx}, σ_{xy}, σ_{yy} are components of the deviatoric stress tensor; *x* and *y* denote the horizontal and vertical

160 coordinates and P is pressure.

161
$$\frac{\partial \sigma_{yy}}{\partial y} + \frac{\partial \sigma_{xy}}{\partial x} = \frac{\partial P}{\partial y} - g\rho(T,P,C) \qquad (eq.\,3)$$

162 where ρ is rock density and depends on rock type(C), temperature(T), and pressure as $\rho(T,P) = \rho_0(1 -$

163 $\xi(T - T_0))(1 + \varsigma(P - P_0))$ where ξ is the coefficient of thermal expansion taken to be 3×10^{-5} K^{-1} for all rock

164 markers and 0 for air/water, ς is the coefficient of compressibility is taken to be 1×10^{-5} MPa[-1] for all rock markers

165   and 0 for air/water, ρ_0 is the reference density at reference temperature ($T_0 = 298.15\ K$) and reference pressure

166   ($P_0 = 10^5 K$).

167   The thermal equation used in the model is as follows:

168
$$\rho C_P \frac{DT}{Dt} = \frac{\partial q_x}{\partial x} + \frac{\partial q_y}{\partial y} + H_r + H_a + H_s \qquad (eq.4)$$

169   where,

170
$$q_x = -k(T,C,y)\frac{\partial T}{\partial x}, \quad q_y = -k(T,C,y)\frac{\partial T}{\partial y} \qquad (eq.5)$$

171    $H_a = T\xi\frac{DP}{Dt}$, $H_s = \sigma_{xx}\dot{\varepsilon}_{xx} + \sigma_{yy}\dot{\varepsilon}_{yy} + \sigma_{xy}\dot{\varepsilon}_{xy} + \sigma_{yx}\dot{\varepsilon}_{yx}$, $H_r = const$ $\qquad (eq.6)$

172   Where$\frac{D}{Dt}$ is the Lagrangian time derivative, and, respectively; $\dot{\varepsilon}_{xx}$, $\dot{\varepsilon}_{xy}$, $\dot{\varepsilon}_{yy}$ are components of the strain rate

173   tensor; q_x, q_y are the components of heat flux in the horizontal and vertical direction; g is the vertical gravitational

174   acceleration; C_P is the isobaric heat capacity; H_r, H_a, H_s denote the radioactive, adiabatic and shear heat production,

175   respectively. $k(T,C,y)$ is the thermal conductivity, a function of composition, depth, and temperature (Table 1).

176   The radioactive heat production H_r is constant for a rock type as mentioned in Table 1.

177   In order to accurately assess thermal maturity, it is crucial to consider the temperature distribution, which

178   necessitates a realistic thermal conductivity profile when modeling thermal maturity. Many geodynamic models

179   assume that thermal conductivity decreases as temperature increases, following a defined relationship (e.g., Clauser

180   and Huenges, 1995). These models typically predict a decrease in thermal conductivity with depth within

181   accretionary wedges, as geothermal profiles tend to increase in temperature with depth. However, empirical data

182   reveal a different trend: thermal conductivity increases with depth, primarily due to sediment porosity influencing

183   shallow thermal conductivity (Henrys et al. 2003, Lin et al. 2014). Additionally, the thermal conductivity values

184   calculated using the Clauser and Huenges model (1995) are significantly higher than those observed at shallow

185   depths (< 3 km). To address these disparities, we incorporate the observed empirical relationship between depth

186   and thermal conductivity from the IODP Site C0002 borehole in the Nankai accretionary wedge into our

187   simulations. By adjusting the thermal conductivity formulation for sediments based on temperature and depth, we

188   aim to replicate the empirical relationship observed in the core samples taken from the borehole at IODP Site C0002

189   (Sugihara et al., 2014) and account for the decrease in thermal conductivity near the surface caused by increased

190   porosity. We modify the thermal conductivity formulation for sediments as a function of temperature and depth as

191   follows.

192
$$k_{sed} = k_0 + \frac{807}{T + 77}\left(1 - \exp\left(\frac{-Z^2}{1.3e^7}\right)\right) \qquad (eq.6)$$

193    $k_0 = 0.96 \; and \; 1.5$ for the wedge sediment and décollement respectively. The larger thermal conductivity of the

194   décollement emulates higher heat transfer in shear zones due to fluid advection (Fig. S1).

195   **3.2 Rheological model**

196   The expression for effective creep viscosities (η_{eff}) is computed as follows.

197
$$\eta_{disl} = 0.5(\dot{\varepsilon}_{II})^{\frac{1}{n}-1} A_D^{\frac{1}{n}} \exp\left(-\frac{E_a + V_a P}{nRT}\right) \qquad (eq.7)$$

198
$$\eta_{diff} = 0.5 \frac{A_D}{S^{n-1}} \exp\left(-\frac{E_a + V_a P}{RT}\right) \qquad (eq.8)$$

$$\eta_{eff} = \left(\frac{1}{\eta_{disl}} + \frac{1}{\eta_{diff}} \right)^{-1} \quad (eq.\,9)$$

199

where R is the gas constant (8.314 J/K/mol), and, A_D, n, m, E_a and V_a are experimentally determined rheological parameters: A_D is the material constant ($Pa^{-n}s^{-1}m^{-m}$), n is the stress exponent, m is the grain size exponent, E_a is activation energy (J/mol) , V_a is activation volume (J/Pa), and S is a stress factor for diffusion creep assumed to be $3 \times 10^4\ Pa$.

200
201
202
203

$$\dot{\varepsilon}_{II} = \sqrt{\frac{\dot{\varepsilon}_{iJ} \cdot \dot{\varepsilon}_{iJ}}{2}} \quad (eq.\,10)$$

204

The model uses visco-plastic rheology to account for both brittle rheology of the shallower and colder rigid lithosphere and deeper, hotter ductile lithosphere and asthenosphere. Using the plastic yield threshold as per the Drucker-Prager criterion we limit effective viscosity as

205
206
207

$$\eta_{eff} \leq \frac{P.\sin\varphi.(1 - \lambda) + C.\cos\varphi}{2\dot{\varepsilon}_{II}} \quad (eq.\,11)$$

208

where C is cohesion and φ is an effective internal angle of friction or $\mu = \tan \varphi$ where is the coefficient of internal friction and λ the fluid pressure ratio assumed to be 0 in all the simulations.

209
210

3.3 Boundary conditions

211

A free-slip boundary condition is implemented on all boundaries, except on the lower boundary, which is permeable in the vertical direction. On the lower boundary we implement an external free slip condition similar to where a free slip condition is satisfied at an external boundary such that

212
213
214

11

215
$$\frac{\partial V_x}{\partial x} = 0, and \ \frac{\partial V_y}{\partial y} = \frac{V_y}{\Delta Y_{external}} \qquad (eq. 10)$$

216 Where, $V_x \ and \ V_y$, are the velocities in the horizontal and vertical directions at the boundary, $\Delta Y_{external}$ is the depth

217 that lies outside the modeling domain, and where free slip condition is maintained. Similarly, we set thermally

218 insulating boundary conditions on all sides except the lower one where the external thermal boundary condition is

219 implemented.

220 **3.4. Surface processes**

221 The rock-water/air boundary is simulated by an adaptive irregular grid that is advected horizontally and vertically

222 and is coupled to the thermomechanical grid which controls the tectonic deformation of the surface. Apart from the

223 tectonic changes, surface processes prescribed in the model can also change the topography. The surface process

224 in the model is controlled by the conversion of rock markers to air/water and vice versa. All sedimentation in the

225 model happens as a focused deposition of sediments from sea to land in morphological depressions (e.g., trench)

226 is modelled as follows (Fig. S2)

227
$$y_{new} = y_{old} + K. y_{fill} \qquad (eq. 11)$$

228 where $K = min \left(\frac{V_{budget}}{V_{basin}}, 1\right)$

229 The shape of the basin and the resolution of the surface grid can lead to overfilling or underfilling when using the

230 equation mentioned above to fill the basin. To address this issue, we calculate the volume of deposited sediments

231 and adjust for any deficit or overfill in the subsequent step. This ensures that, over time, the total amount of

232 sedimentation remains consistent with the prescribed value. However, it is challenging to ensure that all sediments

233 added in a particular step are accommodated within the basins, especially in models with high sedimentation rates

12

234   where significant runoff occurs. Therefore, the sedimentation rates mentioned in this study are computed as

235   effective sedimentation rates after the model runs, rather than being predetermined. We perform multiple models

236   runs (approximately 100) with sedimentation rates uniformly distributed in the range of 0.1-0.9 mm/yr. From these

237   runs, we select models that exhibit appropriate sedimentation rates. This selection process ensures that the average

238   sedimentation rates across all our models (ranging from 0.1-0.9 mm/yr) fall within the observed sedimentation rates

239   in our chosen natural equivalent, the Nankai accretionary wedge in the southwestern subduction margin of Japan

240   (Korup et al., 2014). For more specific information about the model run and prescribed sedimentary conditions,

241   please refer to Table 2

242   **3.5 Thermal maturity calculation**

243   The model computes the %R_o of each marker to estimate the thermal maturity of sediments during the model run

244   using three widely used methods of thermal maturity modelling Easy%R_o (Burnham and Sweeney, 1989, Sweeney

245   and Burnham 1990), Simple%R_o (Suzuki et al., 1993) and Basin%R_o (Nielsen et al., 2017). All the models

246   presented here employ a simplified parallel Arrhenius reaction model, which accommodates an array of activation

247   energies for every component of the kerogen, allowing it to estimate thermal maturity under varying temporal and

248   thermal scales. The Easy%R_o model by Sweeney and Burnham (1990) can be described using the following

249   equations:

250
$$x_i(t) = x_{0i} \, exp\left(-\int A \exp\left(-\frac{E_{ai}}{RT(t)}\right) dt\right) \qquad (eq. 12)$$

251
$$X(t) = \sum_{i=1}^{N} x_i(t) \qquad eq. 13$$

252
$$F(t) = X(t = 0) - X(t) \qquad (eq. 14)$$

13

$$\%R_o = \%R_{o0} \exp(3.7F) \qquad (eq.\,15)$$

253

254 where, x_{oi} are weights of reactions for i^{th} component of the kerogen also described as the stoichiometric coefficient,

255 A is the pre-exponential factor, E_{ai} is the activation energy of the ith component of the kerogen, R is the gas constant,

256 T(t) is the temperature history, F is the amount of fixed carbon as a percentage and $\%R_{o0}$ is the vitrinite reflectance

257 of the immature unaltered sediment. Sweeney and Burnham (1990) provided a set of 20 activation energies (E_{ai})

258 and the stoichiometric coefficient (x_{oi}) listed in Table 3. All thermal models used in this study use the same method

259 of vitrinite reflectance computation albeit with different sets of activation energies, stoichiometric coefficient, pre-

260 exponential factor and $\%R_{o0}$. Table 3 provides a comprehensive list of all these parameters.

261 All these approaches for computing $\%R_o$ yield similar trends albeit with different absolute values. In the interest of

262 clarity, we have mostly illustrated Easy$\%R_o$, which is the most extensively used method for Vitrinite Reflectance

263 computation and hereafter we refer Easy$\%R_o$ as $\%R_o$, unless explicitly stated. $\%R_o$ is set to $\%R_{oo}$ in sediment

264 markers at the start of the model till 2.5 Myr, while $\%R_o$ in markers for other rocks, air, and water is undefined at

265 all times. After 2.5 Myr, the model computes $\%R_o$ on each marker as a function of temperature (T), time (t), and

266 amount of fixed carbon as a percentage (F). The initial $\%R_o$ of newly deposited sediments is computed using an

267 assumed water-sediment interaction temperature assumed to be the same as the thermocline. The thermocline used

268 in the model has been estimated using the data obtained and made freely available by International Argo Program

269 and the national programs that contribute to it for the region near Nankai (Fig. S3; https://argo.ucsd.edu,

270 https://www.ocean-ops.org).

271 **3.5 Model setup**

272 The modelling domain is 3500 km wide and 350 km deep and is divided into 3484 × 401 nodes populated with

273 ~125 million markers (Fig. 1). The high resolution of 220 m (horizontal) × 130 m (vertical) that we assign at the

site of accretionary wedge evolution, decreases steadily toward the edges of the modelling domain to a minimum

resolution of 3000 m x 3200 m. The simulation consists of an oceanic plate converging with a velocity of ~5 cm/yr

and subducting beneath a continental plate (Fig. 1). The convergence is prescribed internally using highly viscous

nodes inside the oceanic and continental plates near the boundary of the models. The oceanic plate consists of a 1-

km-thick upper oceanic crust and a 7-km-thick lower crust (Akuhara, 2018). The thickness of the oceanic lithosphere

depends on its age which is set to 20 Myr at the start of the simulation (Turcotte and Schubert, 2002). The initial

age of the oceanic lithosphere corresponds to the age of the subducting lithosphere in the Nankai subduction margin

(Zhao et al. 2021). Displacement along the megathrust, at the contact between subducting oceanic plate and the

overriding continental plate, occurs in a relatively weak basal layer in accretionary wedges across the globe (Byrne

and Fisher, 1990). We simulate this with a predefined configuration at the interplate, with a 350-meter-thick weak

décollement below a sediment layer that is a km thick. The wedge forms above this interphase by the accretion of

sediments against the continental plate. The continental plate consists of an upper and lower continental crust with

thicknesses of ~20 km and ~15 km, respectively (Akuhara, 2018), and is underlain by a mantle lithosphere of ~25

km. We use a thin (10 km) "sticky air" layer to overlay the top face of the rock strata inside the model which is a

fluid with a low viscosity of $5x10^{17}$ Pa·s, and a low density, similar to air (white in Fig. 1) or water (light blue in

Fig. 1) (Crameri et al., 2012). The transition between the lithosphere and asthenosphere is prescribed to occur at

1300°C. A weak layer is emplaced at the junction of both plates, which fails mechanically and leads to subduction

initiation. All sediments (light and dark brown in Fig. 1) are rheologically identical, but colours are alternated in

time to allow tracking the development of different geological structures. Readers are referred to Table 1 for the

rheological and thermal properties of all the materials used. Note that in our models, we refer to the measure all

distances from the point where the continental and oceanic plates initially and is situated 1850 km from the right

boundary of the modelling area. The terms "landward" and "seaward" indicate the relative direction towards the

continental plate or the oceanic plate, respectively. The "Backstop" refers to the edge of the continental plate that

297   buttresses the wedge and acts akin to an indenter for the accretionary wedge. The "forearc high" represents the

298   highest point in the forearc zone, which includes both the accretionary wedge and the forearc basin.

299

300   *3.6 Experimental Strategy*

301   Here, we present a total of 10 simulations that vary in their effective basal friction or their effective sedimentation

302   rate to discern patterns of thermal maturity evolution in wedge sediments. Models $M_0^{4.5} - M_0^{14.5}$ have no

303   sedimentation and effective internal angle values for the décollement of φ_b= 4.5°, 7°, 9.5°,12° and 14.5°

304   respectively. The chosen range of effective decollement strength is well within the range of values postulated by

305   several studies for the Nankai accretionary wedge (Tesei et al., 2015). The rest of the models ($M_{0.1}^{9.5} - M_{0.9}^{9.5}$) and

306   have a medium-strength décollement and variable effective sedimentation rate ranging from 0.1 to 0.9 mm/yr. In

307   all the models presented in this study, sedimentation is limited to the trench, extending from the sea to the land.

308   Restricting sedimentation to the trench allows us to observe and analyze the length and frequency of thrust sheets,

309   enabling comprehensive investigation of their role in determining sediment trajectories. With these models, we

310   evaluate the particle trajectory and %R$_o$ of accreting sediments as a function of décollement strength and

311   sedimentation rate. To restrict the number of parameters influencing our observations, models have no erosion.

312   Moreover, all models lack surface processes during the first ~2.5 Myr and have sedimentation thereafter. Strain-

313   softening has been modeled as a linear decrease of angle of friction (φ) and cohesion between cumulative strain of

314   0.5 and 1.5. Sediments used in the model have an angle of friction (φ) of 30° before a cumulative strain of 0.5 and

315   a strain-softened value of 20° after a threshold of 1.5 cumulative strain. Strain softening has been used in wedges

316   to mimic the weakening of faults and shear zones due to lubrication with values threshold taken from previous

317   numerical studies (Hickman et al., 1995 , Ruh et. al. 2014).

4. Results

In our models, subduction begins at 0.1 Myr by failure of the weak material between continental and oceanic plate (Fig. 2, Fig. S4-S13 , also see supporting information movies). Continued and sustained accretion of sediments against the deforming continental crust forms the accretionary wedge from the interplate contact landwards. After ~5 Myr, all models develop a distinct wedge in agreement with the critical wedge theory (Davis et al., 1983). Surface slopes, measured by fitting a line in the surface of the wedge for every timestep between 2.5-7.5 Myr and reported as mean ± standard deviation, increase systematically, as effective basal friction increases from ~4.5° to ~14.5° (Fig. 1, Fig S4-S13, Table 2, $M_0^{4.5} - M_0^{14.5}$). Whereas models with a relatively weaker décollement, as $(M_0^{4.5}, \varphi_b = 4.5°)$, have surface slopes of 0.95°± 0.3°, models with very strong décollement, as $(M_0^{14.5}, \varphi_b = 14.5°)$, have slopes as steep as 5.9 ± 1° (Table 2). Our estimations of surface slopes consistently exhibit an excess of approximately 1.5° compared to the surface slopes predicted by the critical wedge theory (Table 2). This is probably due to the penetration of weaker decollement material into high shear zones, resulting in faults that are weaker than the strain-softened wedge material.

Models without trench sedimentation grow solely by accretion of incoming seafloor sediments, with frequent nucleation of frontal thrusts. Models with weaker décollements develop thrust sheets that are lengthier but remain active for shorter periods. This is clear when comparing, for models with increasingly strong décollement $(M_0^{4.5}, M_0^7, M_0^{9.5}, M_0^5, M_0^{14.5})$, the average distance between first and second frontal thrusts are 15.5 ± 7.0 km, 12.1 ± 3.6 km, 8.8 ± 3.3 km, 8.7 ± 2.1 km and 8.0 ± 1.8 km, respectively. Increasing sedimentation rate also leads to an increase in thrust sheet length from 7.3± 1.1 km for model $M_{0.1}^{9.5}$ to 13.8 ± 7.8 km in model $M_{0.9}^{9.5}$.

In models with similar basal friction, models with higher sedimentation rates have lengthier thrust sheets that remain active for longer periods (Table 2). Steeper surface slopes with increased décollement strengths and change

17

341 in thrush sheet length with sedimentation and décollement strength are well-known effects that have been

342 confirmed by previous numerical (Ruh et al., 2012) and analogue (Malavieille and Trullenque, 2009; Storti and

343 Mcclay, 1995) models. All the reported values are mean ± Standard Deviation values recorded between 2.5-7.5

344 Myr in individual models. All models exhibit a temperature gradient that corresponds well with the temperature

345 profile observed in the boreholes at IODP Site C0002 in the Kumano forearc basin, on top of the Nankai

346 accretionary wedge (Fig. S14).

347

348 *4.1 Thermal maturity of the wedge*

349 Sediments are more thermally mature in wedges that have a higher sedimentation rate or décollement strength. For

350 example, the mean %R_o of simulations for wedges with the highest sedimentation is 12% higher (0.75) than in

351 those without sedimentation ($M_0^{4.5}$, Table 2, Fig. 3). Similarly, simulations of wedges with the strongest

352 décollement have the highest mean %R_o (0.94) of all the simulations presented in this study.

353 Thermal maturity values increase with depth and landward distance from the trench to the forearc high

354 irrespective of the decollement strength, sedimentation rates and method of thermal maturity computation (Fig. 3-

355 4). The absolute value of %R_o and the rate at which thermal maturity values increase landward from the trench are

356 larger for wedges with high décollement strength (Fig. 4A). For wedges characterized by the same décollement

357 strength but higher trench sedimentation, we observe that the rate of thermal maturity increases in a landward

358 direction from the trench and remains consistent across these wedges (Fig. 4B). Comparing the values of %R_o

359 along a horizontal marker at the depth of trench in several models emphasizes this result; the model with the highest

360 décollement strength reaches a maximum %R_o of 1.25 and has the highest rate of landward increase in thermal

361 maturity (Fig. 4A). However, all models with similar décollement strength but different sedimentation do not

362 visibly vary in their rate or magnitude of landward increase in thermal maturity. All models show a decrease in

18

363 thermal maturity landward of the forearc high, commonly of 0.2 %R$_o$. Other interesting observations that we

364 explore below are the increased thermal maturity occurring in the vicinity of thrusts and the reversal in sediment

365 maturity around out-of-sequence thrust active over longer times visible across several models (e.g. Fig. 3).

366 The magnitude of %R$_o$ varies consistently among Easy%R$_o$, Simple%R$_o$ and Basin%R$_o$. On average

367 Easy%R$_o$ have the smallest values, followed very closely by Basin%R$_o$ (with an average difference of only 0.02).

368 However, Simple%R$_o$ had the highest average value of thermal maturity, being 0.16 and 0.13 higher than Easy%R$_o$

369 and Basin%R$_o$ (Fig. 3).

4.2 Sediment trajectory inside the wedge

371 In wedges with a higher décollement strength or sedimentation rate, sediments tend to follow high-maturity paths

372 in larger proportions. We demonstrate this effect by creating a map of the thermal maturity of sediments at 7.5 Myr

373 of the model run, mapped to their spatial position at 2.5 My of the model run to analyse the spatial correlation

374 between sediment position (depth and distance) from the trench and thermal maturity (Fig. 5). We also show the

375 mean thermal maturity attained by sediments at a given horizontal distance from the trench during this period by a

376 dashed black line in Fig. 5. The scatter plot shows sharp changes in eventual thermal maturity with horizontal

377 distance from the trench that relate to changes in sediment trajectory. The mean thermal maturity is also variable

378 along the horizontal length of the wedge and has a periodicity (Λ) increasing in distance with higher sedimentation

379 rate but relatively constant with changing basal friction (Fig. 5). The periodicity of mean %R$_o$ was computed by

380 finding the average wavelength of the auto-correlated mean %R$_o$. Whereas the mean thermal maturity has a short

381 periodicity of ~7.2 km for the model $M_0^{9.5}$ with no sedimentation rates, the model $M_{0.9}^{9.5}$ shows the longest periodicity

382 of 21 km. However, for all models with no sedimentation ($M_0^{4.5} - M_0^{14.5}$) , the periodicity remains relatively

383 consistent between the range of 7-8 km.

19

384   Fig. 3 also represents the distribution of trajectories that exist in an accretionary wedge and how these

385   trajectories get impacted under trench sedimentation (a subset of these trajectories can be viewed in the

386   supplementary Fig. S15). Whereas in wedges with weak decollements ($M_0^{4.5}$), none of the shallowest half of

387   incoming sediments reach $\%R_o > 1$ in 5 Myr, 2% of sediments reach this value in wedges with strong décollement

388   ($M_0^{14.5}$). The effects of décollement strength in the thermal maturity of sediments can be quantified as well at deeper

389   levels, with one-eighth vs more than half of the sediments surpassing values of $\%R_o = 1$ for the deepest half of

390   incoming sediments (12% and 54% respectively) in weak vs strong-decollement wedges ($M_0^{4.5}$ vs $M_0^{14.5}$),

391   respectively. In wedges for the model without sedimentation ($M_0^{9.5}$), the top half of the incoming sediments

392   fail to achieve $\%R_o > 1$, as opposed to ~ 15% of them reaching $\%R_o > 1$ in the models with a sedimentation rate

393   of 0.9 mm/yr ($M_{0.9}^{9.5}$). In sum, the proportion of sediments in the top half and bottom half of the wedge that reach

394   high maturity steadily increases with both sedimentation rate and décollement strength (Table 2).

395   *4.3 Patterns of trajectory and thermal maturity in incoming sediments*

396   The diversity in the trajectory of sediments in the wedge leads to a plethora of pathways in which the sediments

397   can become thermally mature and thus introduces epistemic uncertainty in the estimation of maximum exposure

398   temperature. Fig. 6, captures this uncertainty where we plot the maximum exposure temperature as a function of

399    $\%R_o$ for all the models simulated in this study. The colours in for individual markers represent the depth of the

400   markers normalized by the thickness of the wedge represented as Y_n (See Fig S16 for mode details). We find that

401   almost all the models show a remarkable similarity in their relationship between maximum exposure temperature

402   and $\%R_o$ (for individual models please see Fig. S16) and differ mostly in their proportion of sediments with extreme

403   values of $\%R_o$. We observe that the typical uncertainty in maximum exposure temperature increases with an

404   increase in values of $\%R_o$ with ~ 15°C interval at around $\%R_o=0.2$ compared to ~33°C interval at $\%R_o= 3$ (both for

405　95% confidence interval, Fig. 6b). Moreover, we observe that incorporating information about the normalized depth

406　of sediments (Y_n) significantly aids in constraining the maximum exposure temperature. For instance, although the

407　overall uncertainty at %R_o=1, is ~23°C, for sediments with a Y_n of 0.2-0.4, the uncertainty greatly reduces to only

408　~10.5°C. Thus, the range of thermal maturity values for sediments clearly has a large correlation with their

409　trajectories.

410　*4.4 Comparison of Easy%R$_o$, Simple%R$_o$ and Basin%R$_o$*

411　The usage of Easy%R_o, Simple%R_o, and Basin%R_o in our models provides us with a distinct perspective on the

412　comparative (dis)advantages of each method in estimating thermal maturity values. The non-uniqueness of

413　maximum exposure temperatures for the same values of %R_o arises from the variation in sediment trajectory and

414　thermal exposure. This diversity among sediment markers results in multiple markers attaining the same level of

415　thermal maturity. We refer to the range of maximum exposure temperatures corresponding to similar %R_o values

416　as the uncertainty in maximum exposure temperatures. Uncertainty for all three models increases with increasing

417　%R_o from ~20–25°C at ~0.3 to ~35°C at %R_o=3.5 (Fig. 6b). Easy%R_o, probably the best-recognised method of

418　thermal maturity computation, yields the best constraint on uncertainty for very small changes nearing <1 values.

419　For the values of %R_o between 1 and 3, all models yield very similar uncertainty, with Simple%R_o yielding the

420　most constrained exposure temperatures (Fig. 6b). However, beyond %R_o = 3, Simple%R_o becomes unreliable, with

421　uncertainty in exposure temperatures as high as 55°C at %R_o = 4. Easy%R_o yields an uncertainty range of ~37°C

422　till %R_o = 4.4, and starts to be unreliable above this value. Basin%R_o remains consistent until a very high value of

423　%R_o ~ 6, and thus provides the best constraint on the widest range of values of thermal maturity (Fig. 6b).

21

5. Discussion

The thermomechanical models presented in this study provide (a) an explanation for the trend in thermal maturity observed in accretionary wedges, (b) a new venue to explore the uncertainty in the estimation of maximum exposure temperature using vitrinite reflectance, and (c) an estimate of the minimum lateral distance between the trench and the location of a paleo-thermal anomaly on the subduction plate for it to identified after accretion.

5.1 Thermal maturity distribution and importance of thrusting in wedges

Collectively, our results support a general increase of thermal maturity with depth and landward in accretionary wedges. The thermal maturity increase with depth is primarily the result of progressively larger exposures to higher temperatures as depth of burial increases. On the contrary, the landward increase in thermal maturity is caused by the long-term deformation of sediments accumulated at older times and the exhumation of sediments that were underthrusted as they meet the backstop. Our models demonstrate that the rate of landward thermal maturity increase is faster for thicker wedges, both for the case of sediment near the surface and deep inside the wedge (Fig. 4). This can be attributed to a larger proportion of sediments being exposed to higher temperatures over an extended duration within thicker wedges, but validating this result with natural observations remains challenging, given to the very limited availability of thermal maturity data across natural wedges. Accretionary wedges in our models can be simplified as a system where the subducting oceanic plate acts as the primary heat source, while the seafloor acts as a heat sink. The heat generated through other sources such as shear heating, radioactivity, and advection is relatively insignificant compared to the heat originating from the younger oceanic plate. In our simulations, we consider a relatively younger and hotter oceanic plate of approximately 20 Myr, which is consistent with the accretionary wedge in the Nankai region adjacent to the Kumano forearc basin (Zhao et al., 2021). Given that the convergence rate remains constant across all models, the heat received from the oceanic plate should remain relatively similar. However, as the wedge thickness increases, the temperature gradient between the boundaries of

22

447 the wedge must become gentler, resulting in a larger portion of the wedge experiencing elevated temperatures.

448 Moreover, frequent advection from the subduction channel also results in elevated temperatures in the core of the

449 wedge. Finally, models with thicker wedges typically exhibit higher décollement strength, leading to increased

450 shear heating at the base of the wedge. Observational studies conducted by Yamano et al. (1992) on the thermal

451 structure of the Nankai accretionary prism have further highlighted that the landward increase in prism thickness

452 is the most significant factor contributing to temperature variations within the wedge. Consequently, the sustained

453 higher temperatures within thicker wedges over time would lead to a higher rate of landward thermal maturity.

454 Our models show two cases where the above-mentioned trend in thermal maturity is relevantly altered, which we

455 nominate "on-fault increase" and "fault-block inversion". For instance, Fig. 3 shows a steep rise in the thermal

456 maturity of sediments at fault sites. Thermal maturity inversions by thrusting, which are commonplace in

457 accretionary contexts, are the primary cause of thermal maturity differentiation among wedges with similar paleo-

458 thermal structures. During fault-block inversions, the positive gradient of thermal maturity with depth is inverted

459 as relatively mature sediments are thrusted over less mature sediments (Underwood et al., 1992). The strong

460 differentiation in the trajectory of sediments led by thrusting has a larger influence over thermal maturity than their

461 burial depth or their in-wedge location. This novel inference has probably remained concealed thus far due to the

462 large number of parameters that condition thrust development, frequency, length, and thermal state and the lack of

463 high-resolution thermal maturity data.

464 The thermal maturity that incoming sediments reach also varies periodically as a function of thrust frequency. By

465 examining the lateral and vertical position of incoming sediments and their eventual thermal maturity, we can

466 deduce that the overall movement of sediments in the wedge is predominantly layered but not stationary over time.

467 Changes in the depth of the thermal maturity boundary are less frequent and have larger amplitudes with increased

468 décollement strength, and especially, increased sedimentation rates (Fig. 5). The periodicity in the thermal maturity

469   boundary marks the periodic oscillation of the predominant trajectory followed by incoming sediments, i.e. between

470   accretion (low thermal maturity path) and under-thrusting (high-thermal maturity path). As a result, it should also

471   strongly correlate with the periodicity observed in the evolution of forearc topography (Menant et al., 2020) and

472   the frequency of thrust formation in our models. This is expected, given that thrusts are active over longer mean

473   times, and they channel material toward the décollement more efficiently, in wedges with stronger décollement or

474   increased sedimentation. While sediments at internal and higher structural positions of the wedge are translated

475   toward the surface and have a lower thermal maturity, sediments at external and lower structural positions are

476   translated toward the décollement and have a relatively higher maturity. The entire cycle is repeated with the

477   formation of new in-sequence thrust.

478   This is a relevant observation for it typifies the causality of particular sediment grains following a high or low

479   maturity path, a long-standing unanswered question (Miyakawa et al., 2019). We corroborate this observation by

480   analyzing the terminal thermal maturity of sediments across a frontal thrust active at a younger age. An example in

481   Fig. 7 shows the thermal maturity of sediments at ~7.5 Myr across a thrust active at ~4 Myr. Whereas this occurs

482   for all thrusts in the wedge, the frontal thrust is particularly pronounced in partitioning sediments into the high and

483   low maturity paths. Thermal maturity correlates with sediment depth weakly near faults and more strongly away

484   from them. The distance of sediment from the frontal thrust dictates the trajectory of sediment grains, and as a

485   result, the pressure-temperature conditions to which they are exposed.

486   Our results show the need to consider all factors influencing fault frequency when inferring the geothermal history

487   of contractional terrains by means of thermal maturity. In this study, we have considered solely how décollement

488   strength and the rate of trench sedimentation vary the frequency, architecture, and overall behavior of thrusts, and

489   the frontal thrust, as the wedge evolves. Fortunately, this predictive exercise should be relatively straightforward,

490   for the impact of these external factors on the fault structure of wedges has been established (Fillon et al., 2012;

491   Mannu et al., 2016, 2017; Mugnier et al., 1997; Simpson, 2010; Storti and Mcclay, 1995), and the effect of each of

492   these factors can be accounted for when assessing the trajectory of sediments and the distribution of thermal

493   maturity in accretionary wedges. It is nevertheless important to note that the frequency of faults in a wedge can be

494   impacted by many other factors, including hinterland sedimentation (Storti and Mcclay, 1995; Simpson, 2010;

495   Fernández-Blanco et al. 2020), erosion (Konstantinovskaia, 2005; Willett, 1992), and seafloor topography

496   (Dominguez et al., 2000).

497   *5.2. Implications of thermal maturity evolution in a subduction wedge*

498   The main implications of this contribution emerge from its predictive power. Our approach can predict to a precise

499   degree the thermal maturity of sediments and the uncertainty associated with the maximum exposure temperature

500   in accretionary contexts with known structuration. A more accurate quantification of the thermal evolution and

501   thermal state of accreted sediments reduces the uncertainties attached to the location of temperature-led

502   transformations of organic material into hydrocarbons in subduction margins and other accretionary contexts. Such

503   increased accuracy in the distribution of thermally mature sediments may also be applied for improved assessments

504   of the evolution in time of any other geothermal process, including seismic slip, magmatic and metamorphic extent,

505   porosity, compaction, and diagenesis of sediments, and the reconstruction of convergent margins in general

506   (Bostick and Pawlewicz, 1984; Mählmann and Le Bayon, 2016; Rabinowitz et al., 2020; Sakaguchi et al., 2011;

507   Totten and Blatt, 1993; Underwood et al., 1992).

508   Our simulations also imply that the paleo-thermal information stored in the incoming sediments can only be

509   retrieved if sediments are at appropriate locations with respect to emergent thrusts. We illustrate this using two runs

510   of the same model and tracking an artificial thermal anomaly imposed on incoming sediments at two different

511   locations (Fig. 8). This hypothetical thermal anomaly can be conceptualized as any alteration of the thermal

maturity profile of incoming sediments, for example, elevated heat flows by an antecedent magmatic intrusion. While the change in %Ro associated with the short-lived thermal anomaly results in abnormally high values of thermal maturity in both sediment packages, it can only be retrieved for the end-model run of sediments located further from the trench (those in the right panel, Fig. 8B). Contrarily, the end-model run of sediments closer to the trench (those in the left panel, Fig. 8A) shows no signs of discontinuity in the thermal maturity distribution of the wedge. This is because we deliberately placed the thermal anomaly at sites that evolve at two structural locations during the model run, i.e., above and below a yet-undeveloped frontal thrust (Fig. 8). The sediment sector affected by the thermal anomaly closer to the trench is overthrusted by the frontal thrust and remains in a footwall location thereafter (Fig. 8a). In contrast, the homologous sedimentary package further away from the trench is accreted by the frontal thrust and remains in a hanging-wall location (Fig. 8b). Thus, the preservation of the record of an antecedent thermal anomaly is only possible in the former case. We further note that, in our simulations, the entire vertical column of sediments records the thermal anomaly, while in nature, the anomaly may affect only sediments at the deeper locations of the sedimentary pile, which are in turn the sediments that most likely to follow a high-maturity path. We thus regard the possibility of retrieving such antecedent geothermal information as minimal.

Finally, among the three methods of $\%R_o$ computation, Easy$\%R_o$ and Basin$\%R_o$ are more consistent and well-constrained on a wide range of thermal maturities in comparison to Simple$\%R_o$, which seems to be particularly useful for a smaller range of thermal maturity values. This simply illustrates the fact that while Easy$\%R_o$ and Basin$\%R_o$ computation deals with several parallel reactions related to the maturity of kerogen (and hence multiple activation energies), Simple$\%R_o$ is based on best-fitted single activation energy, and hence yields large confidence intervals at the extreme $\%R_o$ values. Additionally, the inclusion of the higher activation energy reactions in Basin$\%R_o$ makes it the best-suited formulation for sediments at the deeper and shear zone sediments which usually get saturated using Easy$\%R_o$.

5.3 Comparisons to previous numerical studies

The thermomechanical models presented in this study offer a dynamic representation of trajectories within the wedge. Although the averaged trends in thermal structure and sediment trajectories remain consistent, there are short-term dynamic fluctuations near the frontal thrust. These fluctuations contribute to a diverse range of sediment paths along the depth of the incoming sediments. Miyakawa et al. (2019) conducted a similar study, modeling vitrinite reflectance using Simple%R_o and a stationary thermal field, which also resulted in an increase in thermal maturity towards the continent and thermal maturity inversions due to thrusting. However, the use of Simple%R_o led to premature saturation and the disappearance of thermal maturity variations at a shallower depth in their model.

We can compare our findings with other geodynamic models that examine the thermal structure of the wedge, although there are only a limited number of numerical models of thermal maturity in wedges. Pajang et al. (2022) recently investigated the distribution of the brittle-ductile transition in wedges and proposed a region dominated by viscous shear near the backstop, with the wedge core reaching temperatures of 450°C and typically containing forearc basins. Although trench sedimentation in our model does not result in the formation of forearc basins, the overall flattening of the wedge slope and the high vitrinite reflectance in the core align with consistent structures. Moreover, the presence of highly mature sediments in the wedge core suggests compacted sediments with greater strength and higher P-wave velocity. Although empirical studies have shown a strong correlation between Vp and thermal maturity estimates for depths of up to 4 km (Baig et al, 2016, Mallick et al. 1995), the exact nature of this correlation may vary depending on the specific location. Nevertheless, the patterns of thermal maturity values in the wedge core in our models also correspond to the patterns of P-wave velocity observed in the Nankai and Hikurangi margins (Górszczyk et al., 2019; Nakanishi et al., 2018; Dewing and Sanei, 2009; Arai et al., 2020).

554   Two modes of sediment trajectory evolution, from incoming sediment to their position inside the wedge, are

555   generally considered; depth dependence sediment trajectories, as observed in studies by Mulugeta and Koyi, (1992)

556   and Hori and Sakaguchi (2011), and crossover exhumation pathways, as illustrated by Konstantinovskaia et al.

557   (2005) and Miyakawa (2019). We consider the latter as non-stationary sediment trajectories that vary with time

558   and cut across sediment trajectories of sediments previously located at the same spatial position. Our models show

559   that both modes of sediment trajectories are valid, and that changes in trajectory patterns leading to path crossovers

560   are controlled by the horizontal distance of sediments from the frontal thrust. Starting at a threshold distance from

561   the trench, sediments at different depths follow laminar paths along different trajectories within the wedge.

562   Laminar-type trajectories can be reproduced in a broad range of simulations and are particularly common in models

563   with low sedimentation and décollement strengths. However, the depth dependence of sedimentary paths varies

564   periodically as a function of distance from the trench of specific sedimentary packages (Fig. 5). This effect, which

565   is particularly marked in the neighbourhood of the frontal thrust, explains the crossover paths for incoming

566   sedimentary packages at similar depths but different horizontal locations (Konstantinovskaia et al. 2005).

567   Therefore, thrust faults in the wedge act as the primary agent controlling whether sediments sustain depth-

568   controlled laminar flow or sediment mixing.

569   *5.4 Comparisons to natural wedges*

570   Our models achieve thermal maturity distributions that are in good agreement with their natural analogues, despite

571   several relevant assumptions. Our models are very simplified with regard to their natural analogues, with

572   assumptions such as no elasticity, predefined décollement, no erosion, and simple and uniform rheology. Also, our

573   models have an insufficient resolution for small-scale fault activity and lack empirical relations to simulate the

574   compaction of sediments and multiscale fluid flow. Although these assumptions hinder a wholesale comparison

575   between our simulations and natural examples of accretionary wedges, we still find an acceptable agreement

between our model and natural observations, primarily due to simulations that have a temperature evolution assimilating empirical data and a fine spatiotemporal resolution. Our estimated %R_o values for the model are in very good agreement with those measured for the borehole C0002 Nankai accretionary wedge by Fukuchi et al. 2009 (Fig. 9). The maximum exposure temperature estimated from the observed thermal maturity for the C0002 borehole also strongly correlates with maximum temperatures recorded on markers in the model with similar thermal maturity with 95% confidence (Fig. S17). However, our result is reliant on the empirical thermal conductivity profiles estimated for the C0002 borehole, which does not show any large thermal discontinuity between the forearc basin and inner wedge that has been observed in fossil accretionary wedges (e.g., Underwood et al. 1989).

Landward increase in thermal maturity is well documented in studies of the Japan trench, at the Miura–Boso plate subduction margin, the fold and thrust belts Western Foothills complex in western Taiwan, the Mesozoic accretionary prism in the Franciscan subduction complex in northern California, as well as Cretaceous Shimanto accretionary complex in Nankai subduction margin (Yamamoto et al. 2017; Sakaguchi et al. 2007; Underwood et al, 1989; Sakaguchi, 1999). The natural wedges mentioned above display vitrinite reflectance values with maximum %R_o values ranging from 0.2 to 4.0 near the surface, which is generally much higher than the near-surface %R_o values observed in our models. Underwood et al. (1989) suggested that this discrepancy is likely due to the ongoing process of progressive exhumation and erosion, leading to the exposure of deeper sections of the accretionary prism over time. As a result, younger wedges, such as those found in the Miura–Boso plate subduction margin, exhibit a much closer resemblance to the %R_o values near the surface of our our models.

On-fault increases in vitrinite reflectance are well also documented in nature, as for boreholes C0004 and C0007, which sample the megasplay fault in Nankai accretionary margin (Sakaguchi et al., 2011). The vitrinite reflectance data from the megasplay and frontal thrusts in Nankai indicate the faults reach a temperature well in excess of 300°C during an earthquake, much larger than the background thermal field. Therefore, on-fault increases in

thermal maturity are comparatively smaller in our simulations and lack the marked increase in %Ro observed at fault sites in nature. We consider this is due to a discrepancy in the rate of change of thermal diffusion occurring in simulated thrusts, given that our models develop much wider fault zones than their natural equivalents. For instance, the location of megasplay fault in C0007 borehole exhibits an unevenness within the high-reflectance zone with a maximum %R_o ~1.9 (Sakaguchi et al., 2011). This is in line with the prediction by Fulton and Harris (2012) about the impact of fault thickness on change in vitrinite reflectance. Natural observations also exhibit a much higher incidence of on-fault increase in thermal maturity compared to our simulations, given that our models do not have sufficient spatial resolution to capture the large number of thin faults that develop inside the wedge. Natural examples of fault-block inversion have been well-documented in natural settings, providing evidence of past thrust activity preserved in the shallower sections of the Nankai accretionary wedge. Sakaguchi (1999) reported the presence of step increments of thermal maturity, similar to increments in vitrinite reflectance in Fig. 3 and 4 across the faults. Other examples are the fault block inversion along the Fukase Fault in the Shimanto accretionary wedge (Ohmori et al., 1997) and the inversion beneath the forearc basin in the Nankai accretionary wedge (Fukuchi et al., 2017).

Our study highlights that paleo-thermal anomalies that extend laterally beyond the average thrust spacing have a significantly higher likelihood of being retained in the final thermal maturity record of the wedge. This allows several inferences. For example, the subduction of the Cretaceous ridge, as identified by Underwood et al. (1993) and Sakaguchi (1999), must have caused a substantial alteration in thermal maturity during the Kula-Pacific subduction in order to be discernible in vitrinite reflectance records. Likewise, we can anticipate the preservation of the paleo-thermal anomaly near Ashizuri in the southern Nankai wedge, which has high thrust frequency, in contrast to that at the Muroto transect, where thrust sheets are widely spaced. In the case of the accretionary wedge adjacent to the Boso peninsula, Kamiya et al. (2017) proposed the emplacement of an ophiolite complex beneath the Miura group. Our findings indicate that the preservation of the thermal-advection heating event coincided with

30

622 a decrease in trench sedimentation. This likely led to an increase in the thrust frequency, which facilitated the

623 preservation of the thermal-advection heating event in the thermal maturity data.

624 **6. Conclusion**

625 This study demonstrates how contractional faults alter the paths of sediments as they accrete and how this

626 fundamentally controls the distribution of the thermal maturity of sediments in accretionary wedges and emphasizes

627 the role that sedimentation rate and interplate contact strength have in such distribution. The increased resolution

628 of our approach leads to findings that have relevant implications. For example, the geothermal history that can be

629 retrieved from the thermal maturity of sediments in drills, i.e., at the shallow wedge, provides, at best, an incomplete

630 record that is skewed towards the thermal evolution of sediments near the trench. Coevally, relevant sectors of

631 sediments located further seaward, when not subducted, follow high-maturity paths that overprint their antecedent

632 thermal history. Finally, this study also provides a first-order uncertainty measure for the thermal maturity of

633 sediments based on the diversity in their trajectory.

634 **Code/Data availability**

635 I2VIS, vitrinite reflection computation and visualization codes would be made available by the corresponding

636 author on request.

637 **Author contribution**

638 UM was responsible for the conceptualization of the work, original draft writing, and administration of the paper.

639 DFB contributed to figure visualization, writing and review of the paper. MK and AM contributed to

640 conceptualization and review. TG provided the I2VIS code and contributed to the review of the paper.

641

Acknowledgments

Competing interests

The authors declare that they have no conflict of interest.

References

1. Akuhara, T. (2018). Receiver Function Image of the Subducting Philippine Sea Plate. Fluid Distribution Along the Nankai-Trough Megathrust Fault off the Kii Peninsula: Inferred from Receiver Function Analysis, 43-64.

2. Arai, R., Kodaira, S., Henrys, S., Bangs, N., Obana, K., Fujie, G., ... & NZ3D Team. (2020). Three-dimensional P wave velocity structure of the Northern Hikurangi margin from the NZ3D experiment: Evidence for fault-bound anisotropy. *Journal of Geophysical Research: Solid Earth*, *125*(12), e2020JB020433.

3. Baig, I., Faleide, J. I., Jahren, J., & Mondol, N. H. (2016). Cenozoic exhumation on the southwestern Barents Shelf: Estimates and uncertainties constrained from compaction and thermal maturity analyses. *Marine and Petroleum Geology*, *73*, 105-130.

4. Bostick, N. H., & Pawlewicz, M. J. (1984). Paleotemperatures based on vitrinite reflectance of shales and limestone in igneous dike aureoles in the Upper Cretaceous Pierre shale, Walsenburg, Colorado.

5. Burnham, A. K., & Sweeney, J. J. (1989). A chemical kinetic model of vitrinite maturation and reflectance. *Geochimica et Cosmochimica Acta*, *53*(10), 2649-2657.

6. Chi, W. C., & Reed, D. L. (2008). Evolution of shallow, crustal thermal structure from subduction to collision: An example from Taiwan. *Geological Society of America Bulletin*, *120*(5-6), 679-690.

7. Clauser, C., & Huenges, E. (1995). Thermal conductivity of rocks and minerals. *Rock physics and phase relations: a handbook of physical constants*, *3*, 105-126.

664   8.   Davis, D., Suppe, J., & Dahlen, F. A. (1983). Mechanics of fold-and-thrust belts and accretionary wedges. *Journal*

665   *of Geophysical Research: Solid Earth*, *88*(B2), 1153-1172.

666   9.   DeMets, C., Gordon, R. G., & Argus, D. F. (2010). Geologically current plate motions. *Geophysical journal inter-*

667   *national*, *181*(1), 1-80.

668   10.   Dewing, K., & Sanei, H. (2009). Analysis of large thermal maturity datasets: Examples from the Canadian Arctic

669   Islands. *International Journal of Coal Geology*, *77*(3-4), 436-448.

670   11.   Dominguez, Stephane, Jacques Malavieille, and Serge E. Lallemand. "Deformation of accretionary wedges in re-

671   sponse to seamount subduction: Insights from sandbox experiments." *Tectonics* 19.1 (2000): 182-196.

672   12.   Fernández-Blanco, D., Mannu, U., Cassola, T., Bertotti G., & Willett SD (2020). Sedimentation and viscosity con-

673   trols on forearc high growth. *Basin Research*, https://doi.org/10.1111/bre.12518

674   13.   Fillon, C., & van der Beek, P. (2012). Post-orogenic evolution of the southern Pyrenees: Constraints from inverse

675   thermo-kinematic modelling of low-temperature thermochronology data. *Basin Research*, *24*(4), 418-436.

676   14.   Fukuchi, M., Nii, T., Ishimaru, N., Minamino, A., Hara, D., Takasaki, I., ... & Tsuda, M. (2009). Valproic acid in-

677   duces up-or down-regulation of gene expression responsible for the neuronal excitation and inhibition in rat cortical

678   neurons through its epigenetic actions. *Neuroscience research*, *65*(1), 35-43.

679   15.   Fukuchi, R., Yamaguchi, A., Yamamoto, Y., & Ashi, J. (2017). Paleothermal structure of the Nankai inner accre-

680   tionary wedge estimated from vitrinite reflectance of cuttings. *Geochemistry, Geophysics, Geosystems*, *18*(8), 3185-

681   3196.

682   16.   Gerya, T. V., & Yuen, D. A. (2003). Characteristics-based marker-in-cell method with conservative finite-differ-

683   ences schemes for modeling geological flows with strongly variable transport properties. *Physics of the Earth and*

684   *Planetary Interiors*, *140*(4), 293-318.

685   17.   Gerya, T. V., & Yuen, D. A. (2003). Rayleigh–Taylor instabilities from hydration and melting propel 'cold plumes'

686   at subduction zones. *Earth and Planetary Science Letters*, *212*(1-2), 47-62.

687   18.   Gerya, T. V., & Meilick, F. I. (2011). Geodynamic regimes of subduction under an active margin: effects of rheo-

688   logical weakening by fluids and melts. Journal of Metamorphic Geology, 29(1), 7-31.

33

689 19. Górszczyk, A., Operto, S., Schenini, L., & Yamada, Y. (2019). Crustal-scale depth imaging via joint full-waveform

690   inversion of ocean-bottom seismometer data and pre-stack depth migration of multichannel seismic data: a case

691   study from the eastern Nankai Trough. *Solid Earth*, *10*(3), 765-784.

692 20. Gool, J. A. V., & Cawood, P. A. (1994). Frontal vs. basal accretion and contrasting particle paths in metamorphic

693   thrust belts. Geology, 22(1), 51-54.

694 21. Heki, K., Miyazaki, S. I., Takahashi, H., Kasahara, M., Kimata, F., Miura, S., ... & An, K. D. (1999). The Amurian

695   Plate motion and current plate kinematics in eastern Asia. *Journal of Geophysical Research: Solid Earth*, *104*(B12),

696   29147-29155.

697 22. Henrys, S. A., Ellis, S., & Uruski, C. (2003). Conductive heat flow variations from bottom-simulating reflectors on

698   the Hikurangi margin, New Zealand. *Geophysical Research Letters*, *30*(2).

699 23. Hickman, S., Sibson, R., & Bruhn, R. (1995). Introduction to special section: Mechanical involvement of fluids in

700   faulting. Journal of Geophysical Research: Solid Earth, 100(B7), 12831-12840.

701 24. Hori, T., & Sakaguchi, H. (2011). Mechanism of décollement formation in subduction zones. *Geophysical Journal*

702   *International*, *187*(3), 1089-1100.

703 25. Kamiya, N., Yamamoto, Y., Wang, Q., Kurimoto, Y., Zhang, F., & Takemura, T. (2017). Major variations in vit-

704   rinite reflectance and consolidation characteristics within a post-middle Miocene forearc basin, central Japan: A

705   geodynamical implication for basin evolution. *Tectonophysics*, *710*, 69-80.

706 26. Kimura, G., Hashimoto, Y., Kitamura, Y., Yamaguchi, A., & Koge, H. (2014). Middle Miocene swift migration of

707   the TTT triple junction and rapid crustal growth in southwest Japan: A review. *Tectonics*, *33*(7), 1219-1238.

708 27. Konstantinovskaia, E., & Malavieille, J. (2005). Erosion and exhumation in accretionary orogens: Experimental and

709   geological approaches. *Geochemistry, Geophysics, Geosystems*, *6*(2).

710 28. Konstantinovskaya, E., & Malavieille, J. (2011). Thrust wedges with décollement levels and syntectonic erosion: A

711   view from analog models. *Tectonophysics*, *502*(3-4), 336-350.

712 29. Korup, O., Hayakawa, Y., Codilean, A. T., Matsushi, Y., Saito, H., Oguchi, T., & Matsuzaki, H. (2014). Japan's

713   sediment flux to the Pacific Ocean revisited. *Earth-Science Reviews*, *135*, 1-16.

714   30. Lin, W., Fulton, P. M., Harris, R. N., Tadai, O., Matsubayashi, O., Tanikawa, W., & Kinoshita, M. (2014). Thermal

715   conductivities, thermal diffusivities, and volumetric heat capacities of core samples obtained from the Japan Trench

716   Fast Drilling Project (JFAST). *Earth, Planets and Space*, *66*(1), 1-11.

717   31. Maehlmann, R. F., & Le Bayon, R. (2016). Vitrinite and vitrinite like solid bitumen reflectance in thermal maturity

718   studies: Correlations from diagenesis to incipient metamorphism in different geodynamic settings. *International*

719   *Journal of Coal Geology*, *157*, 52-73.

720   32. Malavieille, J., & Trullenque, G. (2009). Consequences of continental subduction on forearc basin and accretionary

721   wedge deformation in SE Taiwan: Insights from analogue modeling. *Tectonophysics*, *466*(3-4), 377-394.

722   33. Mallick, R. K., & Raju, S. V. (1995). Thermal maturity evaluation by sonic log and seismic velocity analysis in

723   parts of Upper Assam Basin, India. *Organic Geochemistry*, *23*(10), 871-879.

724   34. Mannu, U., Ueda, K., Willett, S. D., Gerya, T. V., & Strasser, M. (2016). Impact of sedimentation on evolution of

725   accretionary wedges: Insights from high-resolution thermomechanical modeling. *Tectonics*, *35*(12), 2828-2846.

726   35. Mannu, U., Ueda, K., Willett, S. D., Gerya, T. V., & Strasser, M. (2017). Stratigraphic signatures of forearc basin

727   formation mechanisms. *Geochemistry, Geophysics, Geosystems*, *18*(6), 2388-2410.

728   36. Menant, A., Angiboust, S., Gerya, T., Lacassin, R., Simoes, M., & Grandin, R. (2020). Transient stripping of sub-

729   ducting slabs controls periodic forearc uplift. *Nature communications*, *11*(1), 1823.

730   37. Miyakawa, A., Kinoshita, M., Hamada, Y., & Otsubo, M. (2019). Thermal maturity structures in an accretionary

731   wedge by a numerical simulation. *Progress in Earth and Planetary Science*, *6*(1), 1-13.

732   38. Mugnier, J. L., Baby, P., Colletta, B., Vinour, P., Bale, P., & Leturmy, P. (1997). Thrust geometry controlled by

733   erosion and sedimentation: A view from analogue models. *Geology*, *25*(5), 427-430.

734   39. Mulugeta, G., & Koyi, H. (1992). Episodic accretion and strain partitioning in a model sand wedge. *Tectonophysics*,

735   *202*(2-4), 319-333.

736   40. Nakanishi, A., Takahashi, N., Yamamoto, Y., Takahashi, T., Citak, S. O., Nakamura, T., ... & Kaneda, Y. (2018).

737   Three-dimensional plate geometry and P-wave velocity models of the subduction zone in SW Japan: Implications

738   for seismogenesis.

41. Nielsen, S. B., Clausen, O. R., & McGregor, E. (2017). basin% Ro: A vitrinite reflectance model derived from basin and laboratory data. *Basin Research*, *29*, 515-536.

42. Ohmori, K., Taira, A., Tokuyama, H., Sakaguchi, A., Okamura, M., & Aihara, A. (1997). Paleothermal structure of the Shimanto accretionary prism, Shikoku, Japan: Role of an out-of-sequence thrust. *Geology*, *25*(4), 327-330.

43. Pajang, S., Khatib, M. M., Heyhat, M., Cubas, N., Bessiere, E., Letouzey, J., ... & Le Pourhiet, L. (2022). The distinct morphologic signature of underplating and seamounts in accretionary prisms, insights from thermomechanical modeling applied to Coastal Iranian Makran. *Tectonophysics*, *845*, 229617.

44. Platt, J. P. (1986). Dynamics of orogenic wedges and the uplift of high-pressure metamorphic rocks. *Geological society of America bulletin*, *97*(9), 1037-1053.

45. Rabinowitz, H. S., Savage, H. M., Polissar, P. J., Rowe, C. D., & Kirkpatrick, J. D. (2020). Earthquake slip surfaces identified by biomarker thermal maturity within the 2011 Tohoku-Oki earthquake fault zone. *Nature communications*, *11*(1), 533.

46. Ruh, J. B., Kaus, B. J., & Burg, J. P. (2012). Numerical investigation of deformation mechanics in fold-and-thrust belts: Influence of rheology of single and multiple décollements. Tectonics, 31(3).

47. Ruh, J. B., Gerya, T., & Burg, J. P. (2014). 3D effects of strain vs. velocity weakening on deformation patterns in accretionary wedges. Tectonophysics, 615, 122-141.

48. Ruh, J. B. (2020). Numerical modeling of tectonic underplating in accretionary wedge systems. *Geosphere*, *16*(6), 1385-1407.

49. Sakaguchi, A. (1999). Thermal maturity in the Shimanto accretionary prism, southwest Japan, with the thermal change of the subducting slab: fluid inclusion and vitrinite reflectance study. *Earth and Planetary Science Letters*, *173*(1-2), 61-74.

50. Sakaguchi, A., Chester, F., Curewitz, D., Fabbri, O., Goldsby, D., Kimura, G., ... & Yamaguchi, A. (2011). Seismic slip propagation to the updip end of plate boundary subduction interface faults: Vitrinite reflectance geothermometry on Integrated Ocean Drilling Program NanTro SEIZE cores. *Geology*, *39*(4), 395-398.

763   51. Schumann, K., Behrmann, J. H., Stipp, M., Yamamoto, Y., Kitamura, Y., & Lempp, C. (2014). Geotechnical be-

764   havior of mudstones from the Shimanto and Boso accretionary complexes, and implications for the Nankai accre-

765   tionary prism. Earth, planets and space, 66, 1-16.

766   52. Seno, T., Stein, S., & Gripp, A. E. (1993). A model for the motion of the Philippine Sea plate consistent with

767   NUVEL-1 and geological data. *Journal of Geophysical Research: Solid Earth*, *98*(B10), 17941-17948.

768   53. Simpson, Guy DH. "Formation of accretionary prisms influenced by sediment subduction and supplied by sedi-

769   ments from adjacent continents." *Geology* 38.2 (2010): 131-134.

770   54. Storti, F., & McClay, K. (1995). Influence of syntectonic sedimentation on thrust wedges in analogue models. *Geol*

771   55. Sugihara, T., Kinoshita, M., Araki, E., Kimura, T., Kyo, M., Namba, Y., ... & Thu, M. K. (2014). Re-evaluation of

772   temperature at the updip limit of locked portion of Nankai megasplay inferred from IODP Site C0002 temperature

773   observatory. *Earth, Planets and Space*, *66*(1), 1-14.

774   56. Suzuki, N., Matsubayashi, H., & Waples, D. W. (1993). A simpler kinetic model of vitrinite reflectance. *AAPG bul-

775   letin*, *77*(9), 1502-1508.

776   57. Sweeney, J. J., & Burnham, A. K. (1990). Evaluation of a simple model of vitrinite reflectance based on chemical

777   kinetics. *AAPG bulletin*, *74*(10), 1559-1570.

778   58. Tesei, T., Cruciani, F., & Barchi, M. R. (2021). Gravity-driven deepwater fold-and-thrust belts as Critical Coulomb

779   Wedges: Model limitations and the role of friction vs. fluid pressure. *Journal of Structural Geology*, *153*, 104451.

780   59. Totten, M. W., & Blatt, H. (1993). Alterations in the non-clay-mineral fraction of pelitic rocks across the diagenetic

781   to low-grade metamorphic transition, Ouachita Mountains, Oklahoma and Arkansas. *Journal of Sedimentary Re-

782   search*, *63*(5), 899-908.

783   60. Turcotte, D. L., & Schubert, G. (2002). *Geodynamics*. Cambridge university press.

784   61. Underwood, M. B., Moore, G. F., Taira, A., Klaus, A., Wilson, M. E., Fergusson, C. L., ... & Steurer, J. (2003).

785   Sedimentary and tectonic evolution of a trench-slope basin in the Nankai subduction zone of southwest Japan. *Jour-

786   nal of Sedimentary Research*, *73*(4), 589-602.

787   62. Underwood, M. B., O'Leary, J. D., & Strong, R. H. (1988). Contrasts in thermal maturity within terranes and across

788   terrane boundaries of the Franciscan Complex, northern California. *The Journal of Geology*, *96*(4), 399-415.

789   63. Underwood, M. B. (1989). Temporal changes in geothermal gradient, Franciscan subduction complex,

790   northern California. *Journal of Geophysical Research: Solid Earth*, *94*(B3), 3111-3125.

791   64. Wenk, L., & Huhn, K. (2013). The influence of an embedded viscoelastic–plastic layer on kinematics and mass

792   transport pattern within accretionary wedges. *Tectonophysics*, *608*, 653-666.

793   65. Willett, S. D. (1992). Dynamic and kinematic growth and change of a Coulomb wedge. In *Thrust tectonics* (pp. 19-

794   31). Dordrecht: Springer Netherlands.

795   66. Yamano, M., Foucher, J. P., Kinoshita, M., Fisher, A., Hyndman, R. D., Leg, O. D. P., & Party, S. S. (1992). Heat

796   flow and fluid flow regime in the western Nankai accretionary prism. *Earth and Planetary Science Letters*, *109*(3-

797   4), 451-462.

798   67. Zhao, D., Wang, J., Huang, Z., & Liu, X. (2021). Seismic structure and subduction dynamics of the western Japan

799   arc. *Tectonophysics*, *802*, 228743.

800

801

802

803

804

805

806

807

Rock Type	Reference Density(ρ_o) (kg/m³)[a]	Cohesion (MPa)[b]	Angle of friction (°)[c]	Thermal Conductivity (W/ (m K)) [d]	Flow law[e]	E (kJ/mol)	n	H_r (μW/ kg)	A_D (Pa⁻ⁿ s⁻¹)	V (J µPa⁻¹ mol⁻¹)
Water	1000	0	0	20		0	0	0	0	0
Air (Sticky-air)	0	0	0	20		0	0	0	0	0
Décollement	2600	0.001	4.5-14.5	$(1.5+807/ (T+77))*$ $(1-\exp (-Z^2/1.3e7))$	Wet quartzite	154	2.3	1.5	1.97×10^{17}	8
Sediments1	2600	1/0.05	30/20*	$(0.96+807/ (T+77))*$ $(1-\exp (-Z^2/1.3e7))$	Wet quartzite	154	2.3	1.5	1.97×10^{17}	8
Sediments2	2600	1/0.05*ᵇ	30/20*	$(0.96+807/ (T+77))*$ $(1-\exp (-Z^2/1.3e7))$	Wet quartzite	154	2.3	1.5	1.97×10^{17}	8
Upper Continental Crust	2700	10	31	$0.64+807/ (T+77)$	Wet quartzite	300	2.3	1	1.97×10^{17}	12
Lower Continental Crust	2800	10	31	$0.64+807/ (T+77)$	Plagioclase An75	300	3.2	1	4.8×10^{22}	8
Upper Oceanic Crust	3000	10	31	$1.18+474/ (T+77)$	Wet quartzite	300	2.3	0.25	1.97×10^{17}	8
Lower Oceanic Crust	3000	10	31	$1.18+474/ (T+77)$	Plagioclase An75	300	3.2	0.25	4.8×10^{22}	8
Mantle Lithosphere	3300	10	31	$0.73+1293/ (T+77)$	Dry olivine	532	3.5	0.022	3.98×10^{16}	8
Asthenosphere	3300	10	31	$0.73+1293/ (T+77)$	Dry olivine	532	3.5	0.022	3.98×10^{16}	8

*Strain-softened Cohesion/Coefficient of friction.
*We have assumed the flow law parameters such as A_D, E, V and n to be the same for dislocation and diffusion creep.
T is Temperature in Kelvin, Z is the depth from the seafloor
The reference temperature for densities have been taken as the average temperature of the rock type.
[a]Reference for Densities: Turcottee & Schubert, 2002; Gerya & Meilick, 2011
[b]Reference cohesion values for sediments Schumann et al. 2014
[c]Reference for angle of frictions Schumann et al. 2014, Ruh et. al 2014, Gerya & Meilick, 2011
[d]Reference for thermal conductivity: Clauser & Huenges. (1995) , Sugihara et al., 2014
[e]Reference for flow laws and radiogenic heat production: Ranalli 1995, Gerya & Meilick, 2011

810

811

Table 2: Model runs and their specific characteristic observations

Models	φ_b	φ / φ_{ss}	λ	SR	L	$\beta(°)$	$\alpha(°)$	α predicted (φ_{ss}/φ) (°)	D	$<R_o\%>$	$\%_{top\text{-}half}$	$\%_{Bottom\text{-}half}$
$M_0^{4.5}$	4.5°	30°/20°	0	None	123.2±15.7	4.2±0.6	0.95±0.3	0.03±0.2/-1.3±0.3	15.5±7.0	0.54	0.0	12.7
M_0^7	7°	30°/20°	0	None	97.7±9.9	4.9±0.8	2.6±0.8	0.97±0.2/-0.95± 0.3	12.1±3.6	0.60	0.0	22.5
$M_0^{9.5}$	9.5°	30°/20°	0	None	77.8±4.8	5.3±0.8	3.7±0.9	2.1±0.4/-0.32±0.3	8.7±2.1	0.67	0.0	31.3
$M_{0.1}^{9.5}$	9.5°	30°/20°	0	0.1	76.1±5.9	5.0±0.9	2.3±0.7	2.3±0.4/-0.12±0.3	7.3±1.1	0.71	0.1	35.3
$M_{0.3}^{9.5}$	9.5°	30°/20°	0	0.3	79.3±8.2	4.9±0.9	2.0±0.5	2.3±0.4/-0.1±0.3	7.8±2.5	0.69	0.1	32.0
$M_{0.5}^{9.5}$	9.5°	30°/20°	0	0.5	79.9±7.4	4.9±0.8	2.1±0.5	2.3±0.4/-0.1±0.2	9.5±4.0	0.71	2.7	34.4
$M_{0.7}^{9.5}$	9.5°	30°/20°	0	0.7	81.3±10.5	5.0±0.9	2.1±0.5	2.3±0.7/-0.11±0.3	9.9±5.0	0.73	4.2	41.5
$M_{0.9}^{9.5}$	9.5°	30°/20°	0	0.9	82.5±11.0	5.0±0.9	2.3±0.7	2.2±0.4/-0.16±0.3	13.8±7.8	0.75	14.6	51.8
M_0^{12}	12°	30°/20°	0	None	71.6±5.0	5.6±1.0	5.1±1.0	3.5±0.6/0.4±0.4	8.8±3.3	0.83	1.2	40.6
$M_0^{14.5}$	14.5°	30°/20°	0	None	62.7±6.0	5.9±1.0	6.7±1.4	5.1±0.8/1.2±0.4	8.0±1.8	0.94	2.0	54.0

φ_b is décollement Strength (internal angle of friction).
φ Sediment Strength.
φ_{ss} Sediment Strength (Strain weakened)/ (internal angle of friction).
SR Average Sediment rate (mm/yr).
λ is pore-fluid pressure ratio.
L Average Length of the wedge (in km) between ~2.5-7.5Myr. Length of the wedge is computed as the distance between trench and backstop(set at 1850 km from the right edge of the modelling domain).
β Average basal dip angle β (in degrees) between ~2.5-7.5Myr measure by fitting a line in the basal surface.
α Average surface slope angle α (in degrees) between ~2.5-7.5Myr measure computing the slope of fitting the best fitted line in the surface.
D Average Distance between the first and second frontal thrust between ~2.5-7.5Myr (in km). The frontal thrust is always identified from the trench. The send thrust is identified by the high strain rate and deviation of the weak décollement material from the trend of oceanic plate.
α predicted (φ_{ss}/φ) is the surface slope predicted using critical wedge theory using the **β** observed in the model and sediment strength (Initial /Strain weakened).
T Average time a frontal thrust remains active between ~3.5-7.5Myr.
$<R_o\%>$ Average vitrinite reflectance of the wedge between ~3.5-7.5 Myr.
$\%_{top}$ Proportion of >1 eventual **$R_o\%$ (vitrinite reflectance at 7.5 Myr)** at shallow half of the incoming sediment at 2.5 Myr.
$\%_{bottom}$ Proportion of >1 eventual **$R_o\%$ (vitrinite reflectance at 7.5 Myr)** at deep half of the incoming sediments.

*Please see Fig. S18 for details on the various measurement done on the wedge.

815 ***Table 3: Parameters for Easy%R_o, Simple%R_o and Basin%R_o vitrinite reflectance model.***

S. No.	Stoichiometric Coefficient for Easy%R_o (x_{0i_Easy})	Activation Energy for Easy%R_o (kJ/mol) (E_{ai_Easy})	Stoichiometric Coefficient for Simple%R_o (x_{0i_Simple})	Activation Energy(E) for Simple%R_o (E_{ai_Simple})	Stoichiometric Coefficient for Simple%R_o (x_{0i_Basin})	Activation Energy(E) for Basin%R_o (kJ/mol) (E_{ai_Simple})
1	0.0300	142256	1	1.38e5	0.0185	142256
2	0.0300	150624	-	-	0.0143	150624
3	0.0400	158992	-	-	0.0569	158992
4	0.0400	167360	-	-	0.0478	167360
5	0.0500	175728	-	-	0.0497	175728
6	0.0500	184096	-	-	0.0344	184096
7	0.0600	192464	-	-	0.0344	192464
8	0.0400	200832	-	-	0.0322	200832
9	0.0400	209200	-	-	0.0282	209200
10	0.0700	217568	-	-	0.0062	217568
11	0.0600	225936	-	-	0.1155	225936
12	0.0600	234304	-	-	0.1041	234304
13	0.0600	242672	-	-	0.1023	242672
14	0.0500	251040	-	-	0.076	251040
15	0.0500	259408	-	-	0.0593	259408
16	0.0400	267776	-	-	0.0512	267776
17	0.0300	276144	-	-	0.0477	276144
18	0.0200	284512	-	-	0.0086	284512
19	0.0200	292880	-	-	0.0246	292880
20	0.0100	301248	-	-	0.0096	301248
A_{Easy} = 1e13 and %R_{o0} = 0.2, A_{Simple} = 1e13 and %R_{o0} = 0.2, A_{Basin} = 9.7029e12 and %R_{o0} = 0.2104						

816

817

818

Fig. 1:

Initial model setup. A. The lithological and geothermal map of the whole computational domain with boundary conditions. B. The zoomed lithological and geothermal map of the inset illustrates the junction of continental and oceanic plates. The colors represent different lithology of the materials used in the models, with upper and lower crust represented by light and dark grey, upper and lower oceanic crust represented by dark and light green. The arrows around the computational domain represent the imposed boundary conditions, while the white contour lines (dashed in the zoomed panel) show the geothermal gradients used for the initial model. The numbers on the white contour lines represent the temperature values in ℃ for the contour.
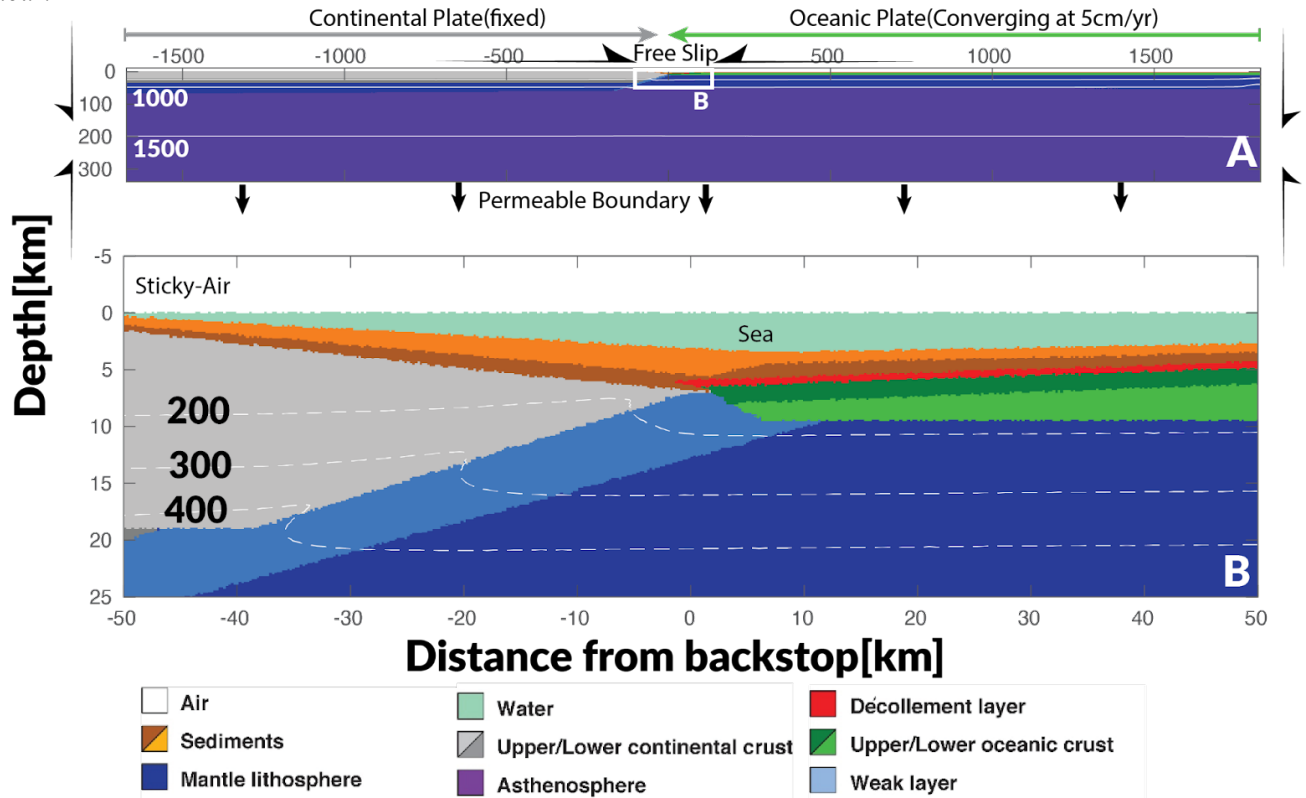
827　h

828

829

830

831

832

833

834

835 ***Fig. 2:***
836 *Typical thermomechanical evolution of the accretionary wedge for model. The illustrated Figure is for the model $\mathbf{M_0^7}$ at (a)0.5*
837 *Myr (b)2.5 Myr (c)5.0 Myr (d) 7.5 Myr. Similar Figures for other models have been illustrated in supplementary images. The*
838 *colormap for the panels is same as Figure 1.*
839
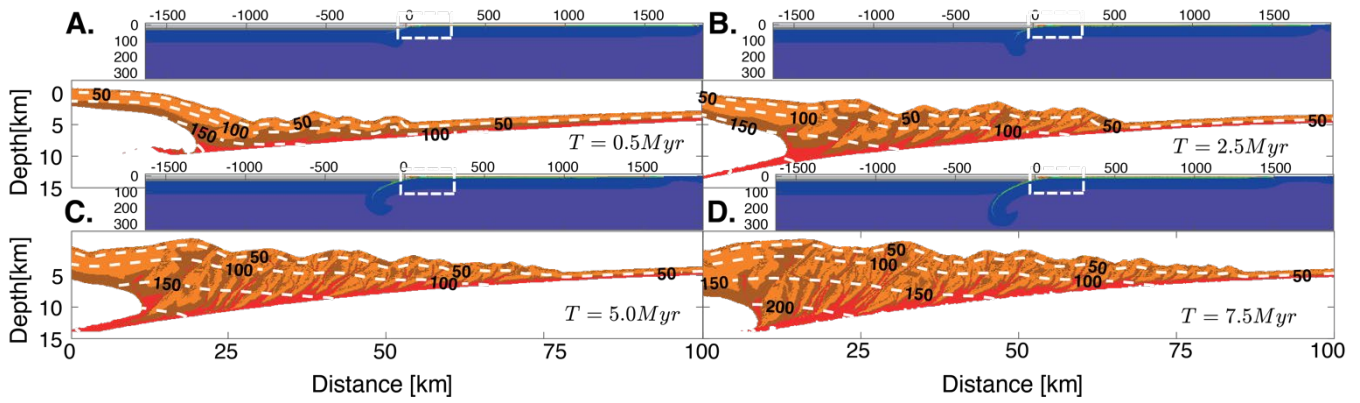
Fig. 3:

861 *Distribution of thermal maturity for different models at ~6.0 Myr (3.5 Myr of thermal maturation). Panels A1-A5 show the*
862 *thermal maturity distribution (computed using Easy%R$_o$) in subduction wedges of models as a function of décollement strength*
863 *, respectively. A6-A10 show the thermal maturity distribution in subduction wedges of models function of sedimentation rae ,*
864 *respectively. The grey color of the markers indicate that no thermal maturity change in these sediments have not occurred.*
865 *B1-B10 and C1-C10 similarly show the thermal maturity distribution in subduction wedges computed using Simple%R$_o$ and*
866 *Basin%R$_o$, respectively.*

867
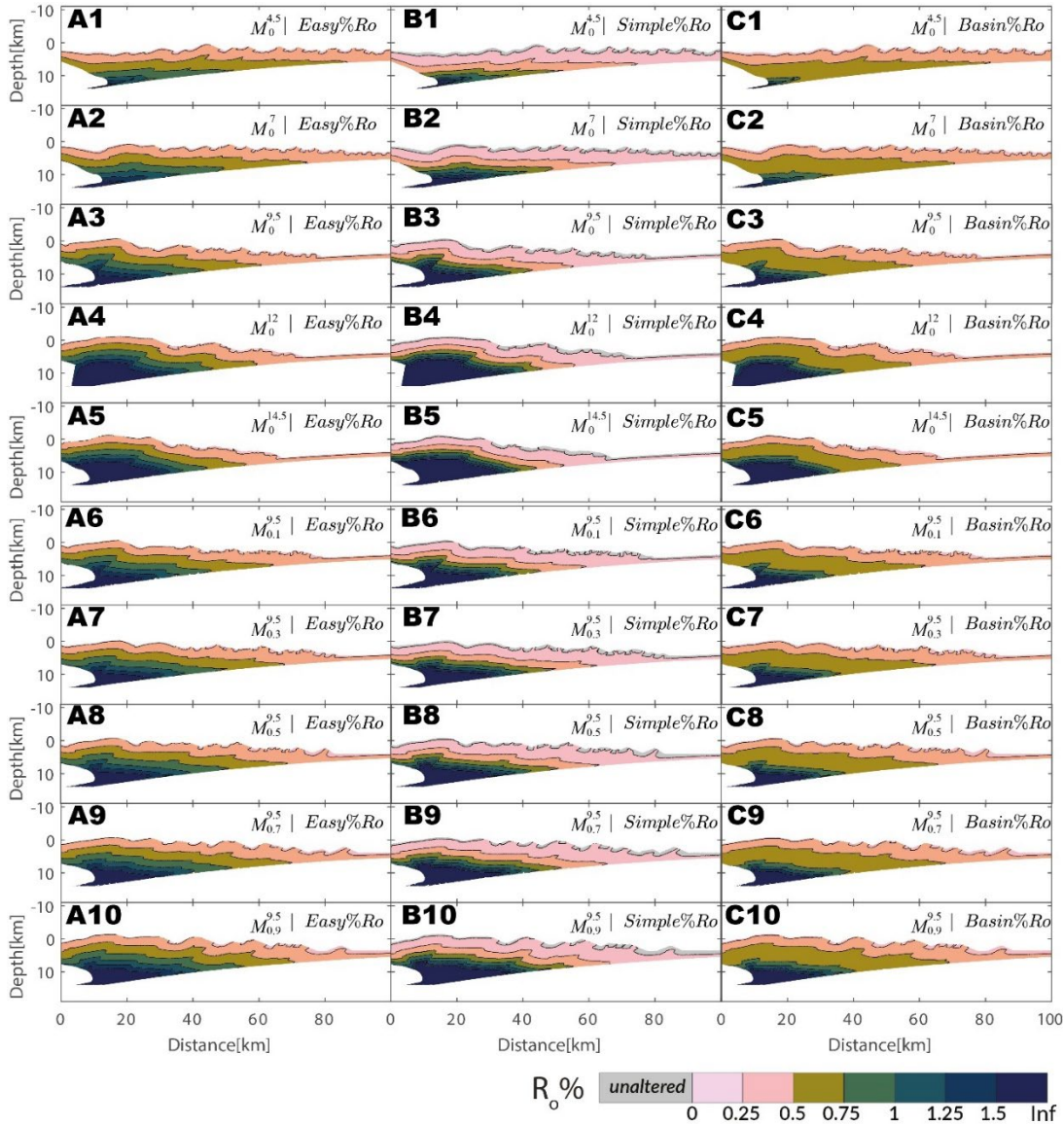
Fig. 4:

The variation of $\%R_o$ for a horizon as indicated by the orange band in the inset at 7.5 Myr. Panel A1 and A2 shows all the models with different decollement strength. Panel B1 and B2 shows all the models with different sedimentation rates. Horizons in panel A1 and B1 are located at 1 km depth from the surface, whole in panel A2 and B2 the horizons are horizontal zones located at the trench depth. The horizontal distance from the backstop is normalized by the wedge length. Horizontal distance 0 represents the fixed backstop and 1 represents the trench.
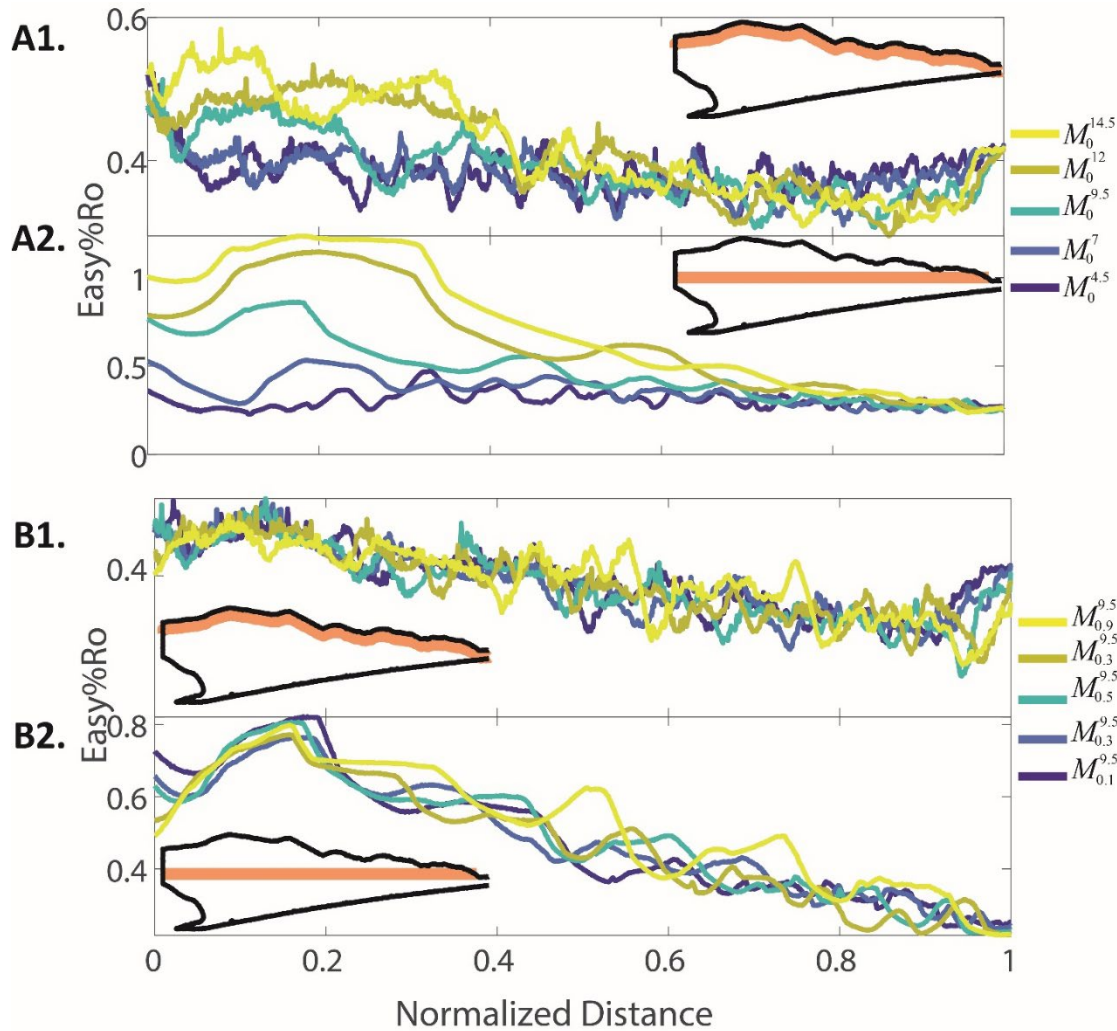
Fig. 5:

881 *Map of thermal maturity at 7.5 Myr mapped to sediments at 2.5 Myr. Panel A1-A5,B1-B5 show the mapping for models - and*
882 *- respectively. The vertical axis (distance from the oceanic plate) has been corrected for the bending of the plate. The horizontal*
883 *axis represents the distance of sediments from the trench. The grey colour of the markers indicates that these sediments have*
884 *been eroded/reworked due to slope failure. The broken black line represents the mean $\%R_o$ attained sediment at a given*
885 *distance from the trench. Λ represents the horizontal periodicity in mean $\%R_o$ for the given model.*

886

912

913
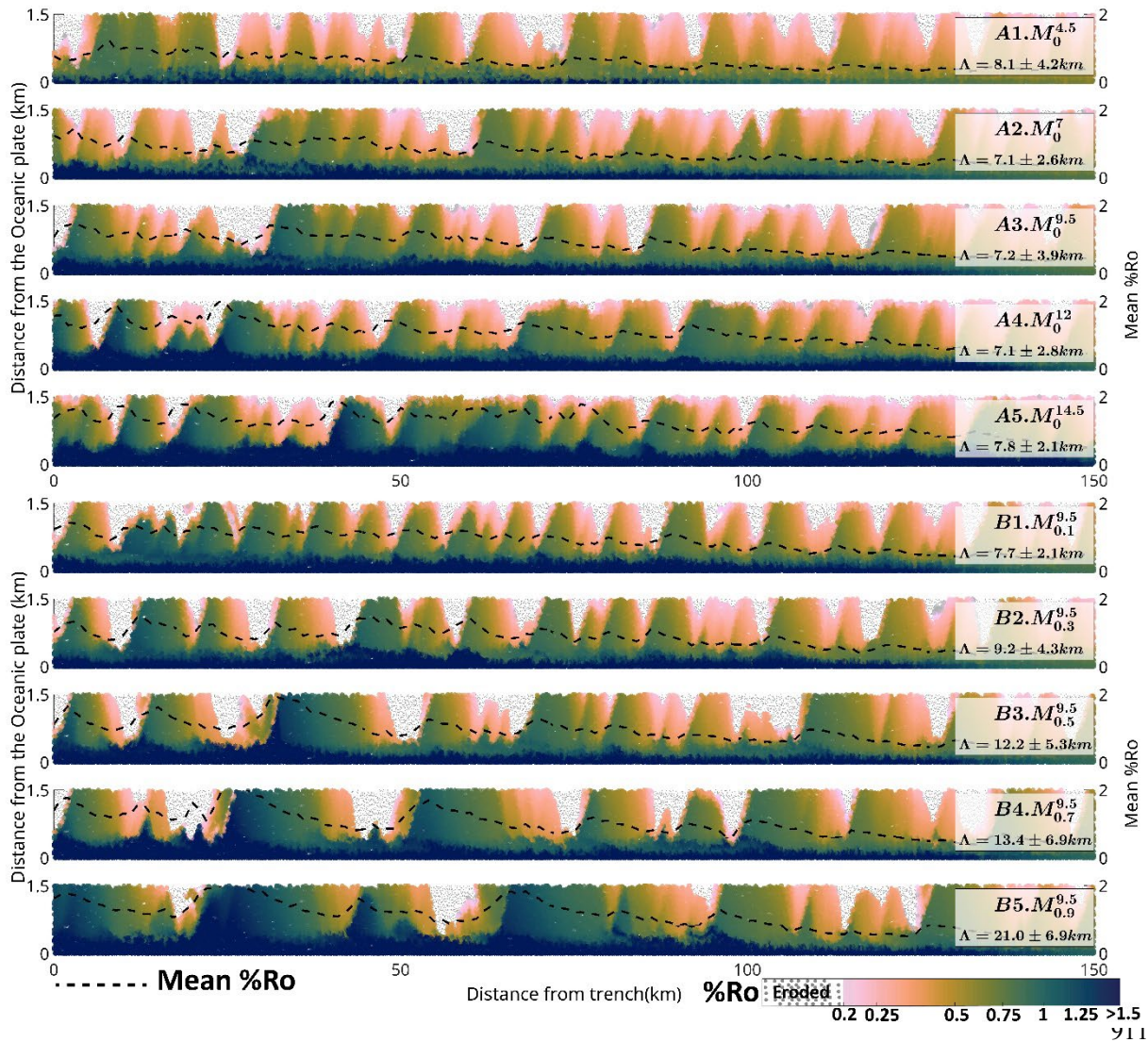
Fig. 6:

915 *A. Vitrinite Reflectance (%R_o) vs Maximum Exposure temperature in all models. The colours in panel A represent the depth*
916 *of the sediments at 7.5 Myr normalized by the thickness of the wedge (Y_n). B. Range of 95% CI for Easy%Ro, Simple%Ro and*
917 *Basin%Ro. Y_n is the depth of the marker from the surface normalized by the thickness (vertical extent) of the wedge at the*
918 *location of the marker. Please see panel B of Fig. S16 for computation of Y_n*
919

920
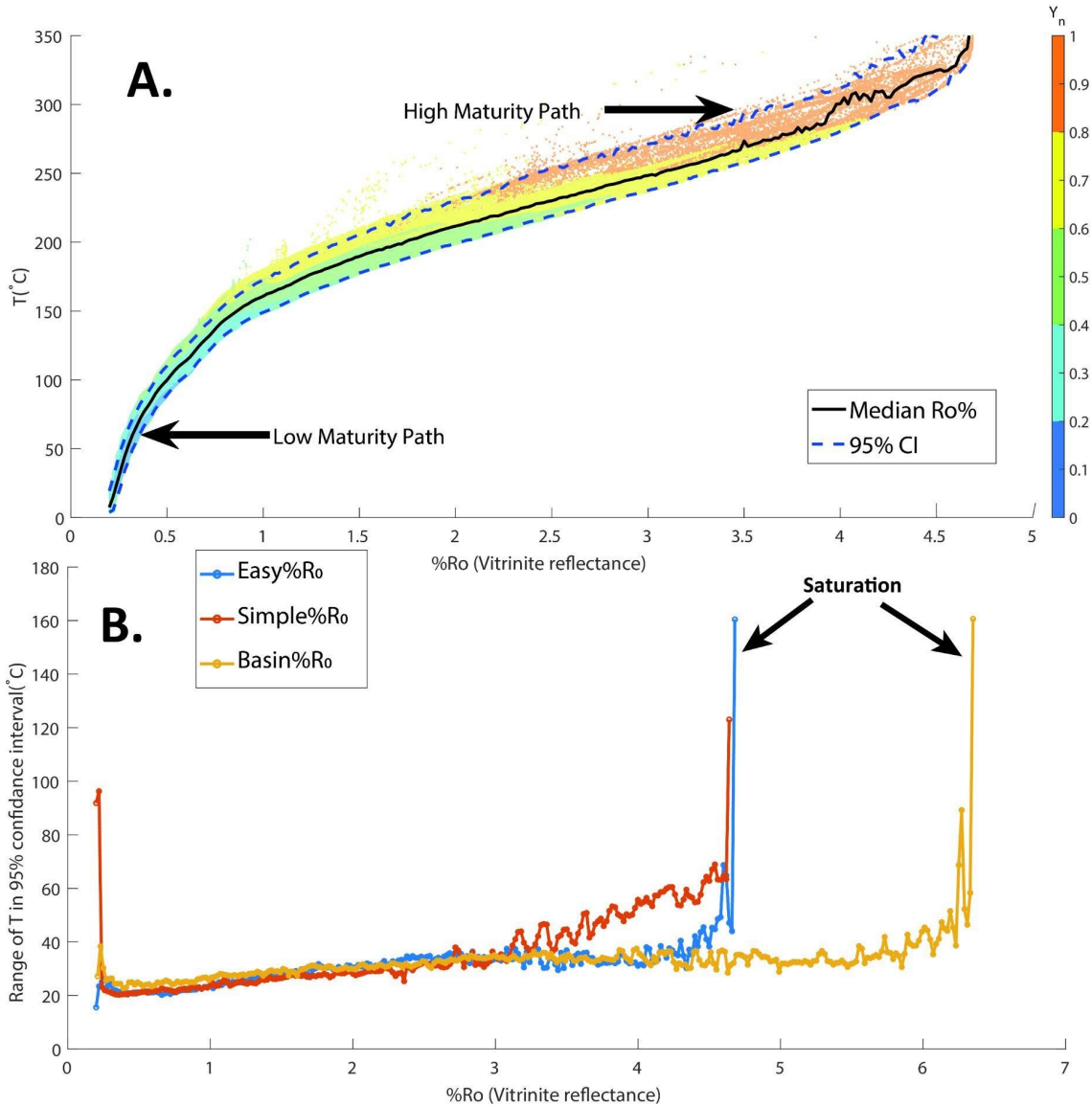
Fig. 7:

922 *Mapping of eventual thermal maturity (vitrinite reflectance at 7.5Myr) to the location of same markers at ~4Myr in model .*
923 *Panel A shows the values of thermal maturity for the markers while the lithology of the wedge is shown in panel B. The half*
924 *arrow represents the active frontal thrust. The sediments which were eroded by 7.5Myr but exist at 4Myr have been markers*
925 *eroded using dotted grey points.*
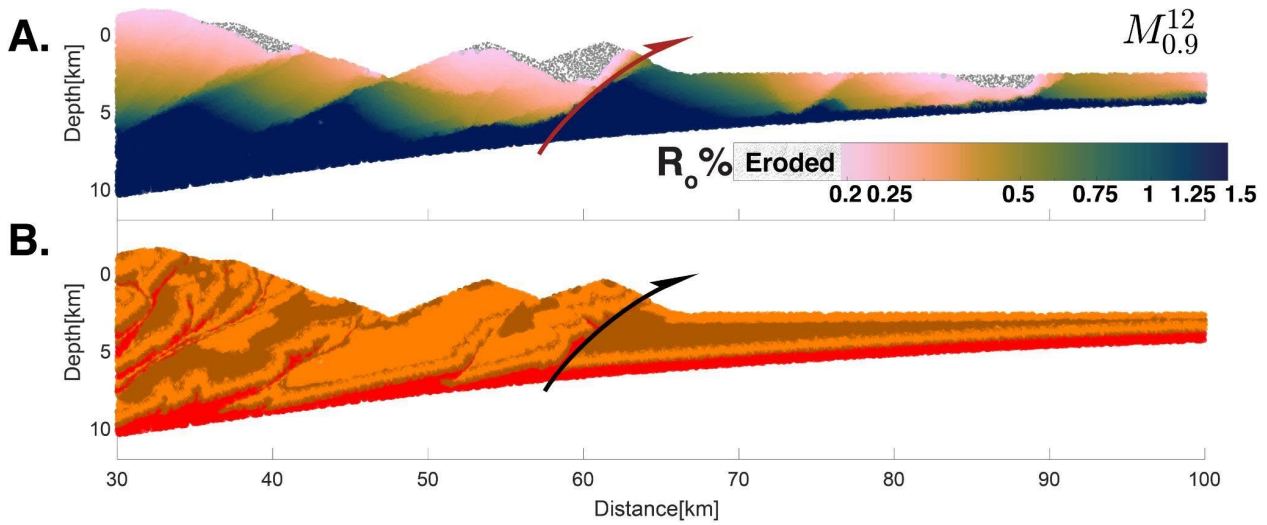
926

927

928

929

930

931

932

933

934

935

936

937

938

939

940

941

Fig. 8:

Position dependency of thermal maturity preservation. A1. Distribution of %R₀ at 2.5 Myr with a paleo-thermal anomaly emplaced at 130-145 km from the backstop. A2. The evolution of the emplaced paleo-thermal anomaly from 2.5 Myr to 6.5 Myr in case 1. A3. Distribution of %R₀ at 2.5 Myr. B1. Distribution of %R₀ at 2.5 Myr with a paleo-thermal anomaly emplaced at 145-160 km from the backstop. B2. The evolution of the emplaced paleo-thermal anomaly from 2.5 Myr to 6.5 Myr in case 2 B3. Distribution of %R₀ at 2.5 Myr with a paleo-thermal anomaly emplaced at 145-160 km from the backstop.

49

952

953
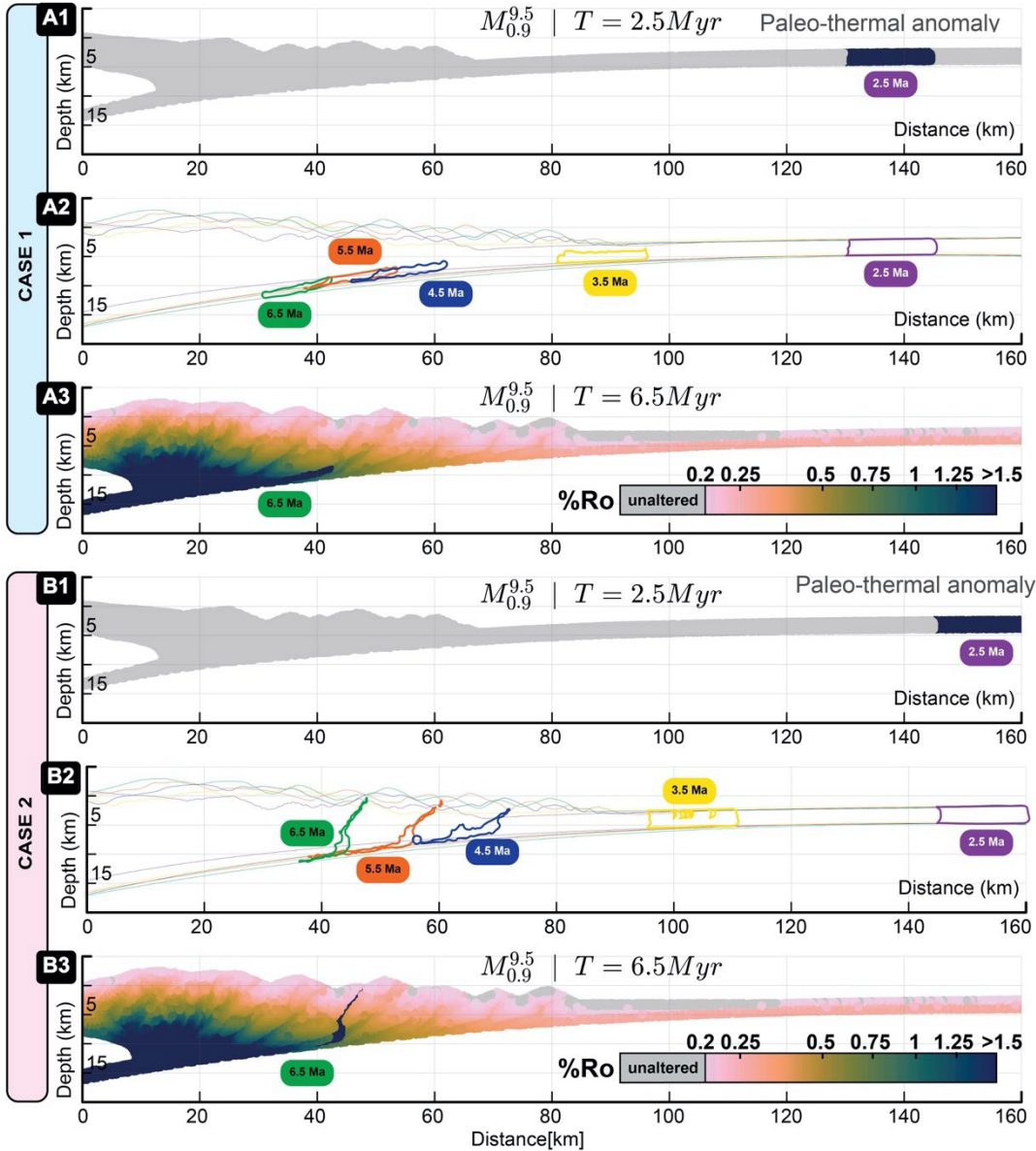
Fig. 9:

Depth vs Thermal maturity (%R$_o$). The shaded (in voilet) region shows the range of observed R$_o$% (mean±1SD) from the C0002
borehole ,colored lines represent the values in models sampled from a 10 km wide hypothetical borehole 20km seaward of the
backstop as shown in the inset .

958
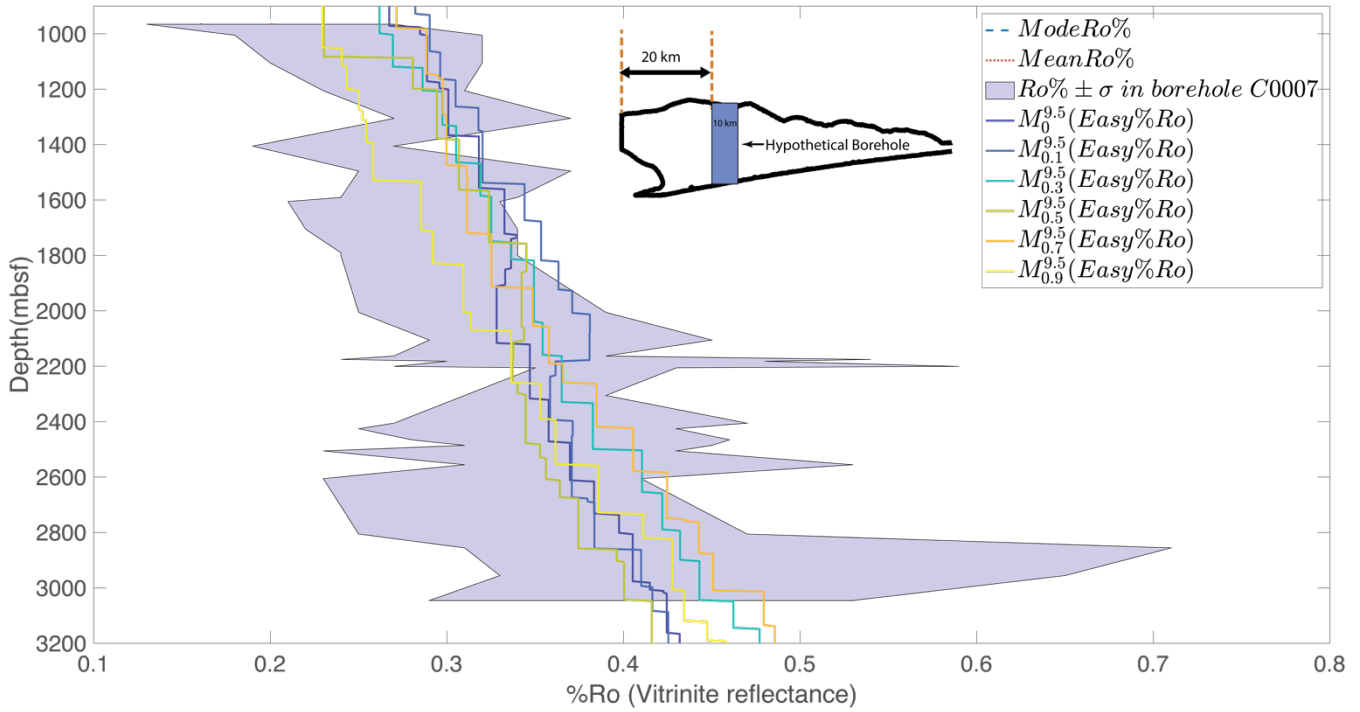
959

960

961

962

963   **Supplementary Figures**

964   **Fig. S1:**

965   *Typical Distribution of thermal conductivity in wedge*

966

967

968

969

970

971

972

973

974

975

976

977

978

979

980
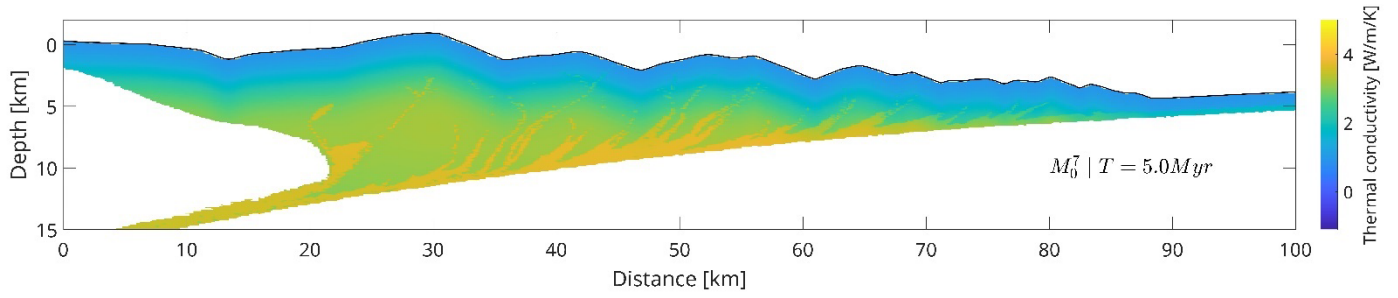
Fig. S2:

982 *Scheme of trench sedimentation in models (taken from (Mannu et al., 2017))*
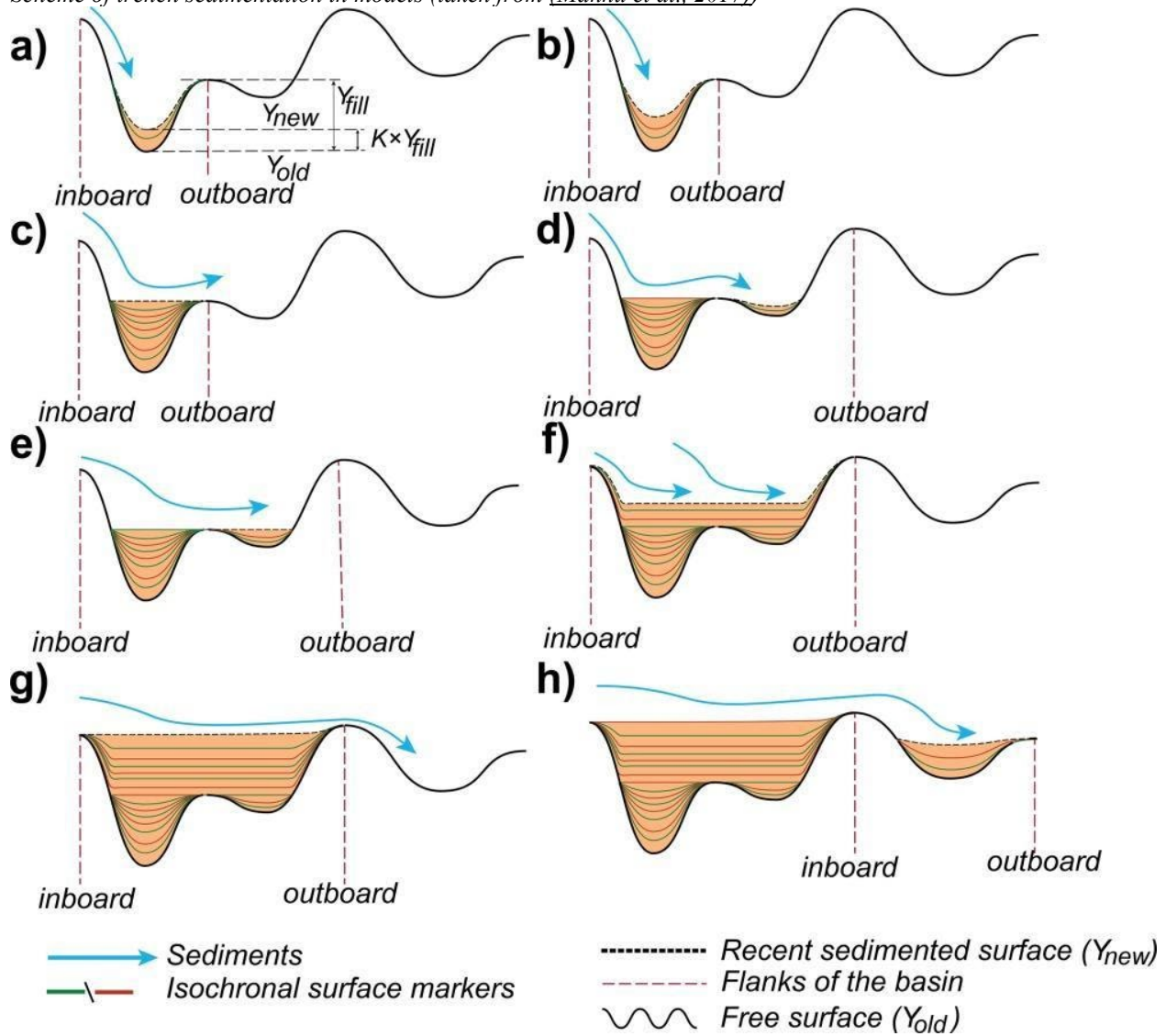
983
984
985
986
987
988

52

989   **Fig. S3:**

990   *Plot of Temperature vs Depth profile in for water-sediment interaction using the data from the International Argo Program*
991   *and the national programs that contribute for the location(represented by the white square) given in the inset The magenta*
992   *circle **represents** the Temperature vs Depth profile from the data while the black line is the fitted thermocline used in our*
993   *models for water-sediment thermal interaction.*
994
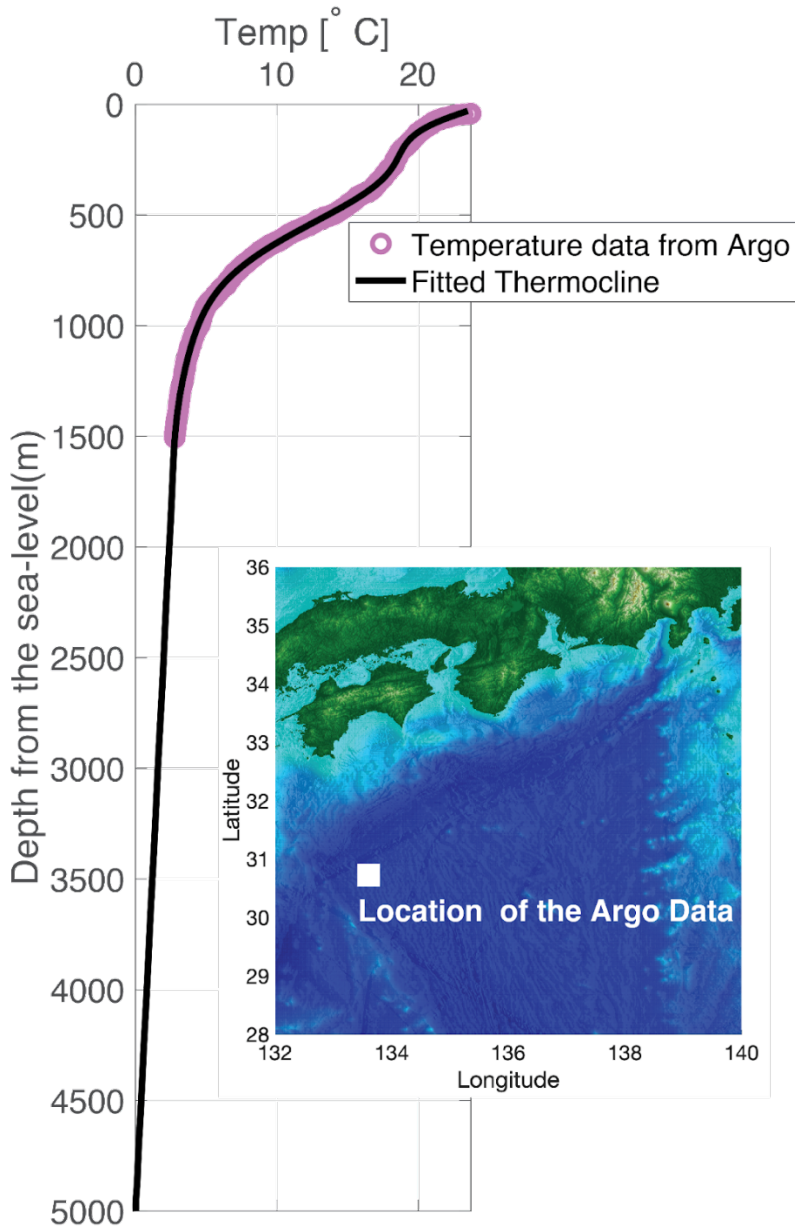
995

Fig. S4:

Typical thermomechanical evolution of the accretionary wedge for model $M_0^{4.5}$ at 0.5 Myr, 2.5 Myr, 5.0 Myr and 7.5 Myr of lithological evolution (Panel A-D). The dashed white lines represent the contours of the temperature field. The colormap for the first 4 panels is same as Figure 1. The last panel represents thermal maturity values at ~7.5 Myr computed using Easy%R$_o$. The colormap for Panel E is same as that of Figure 3.
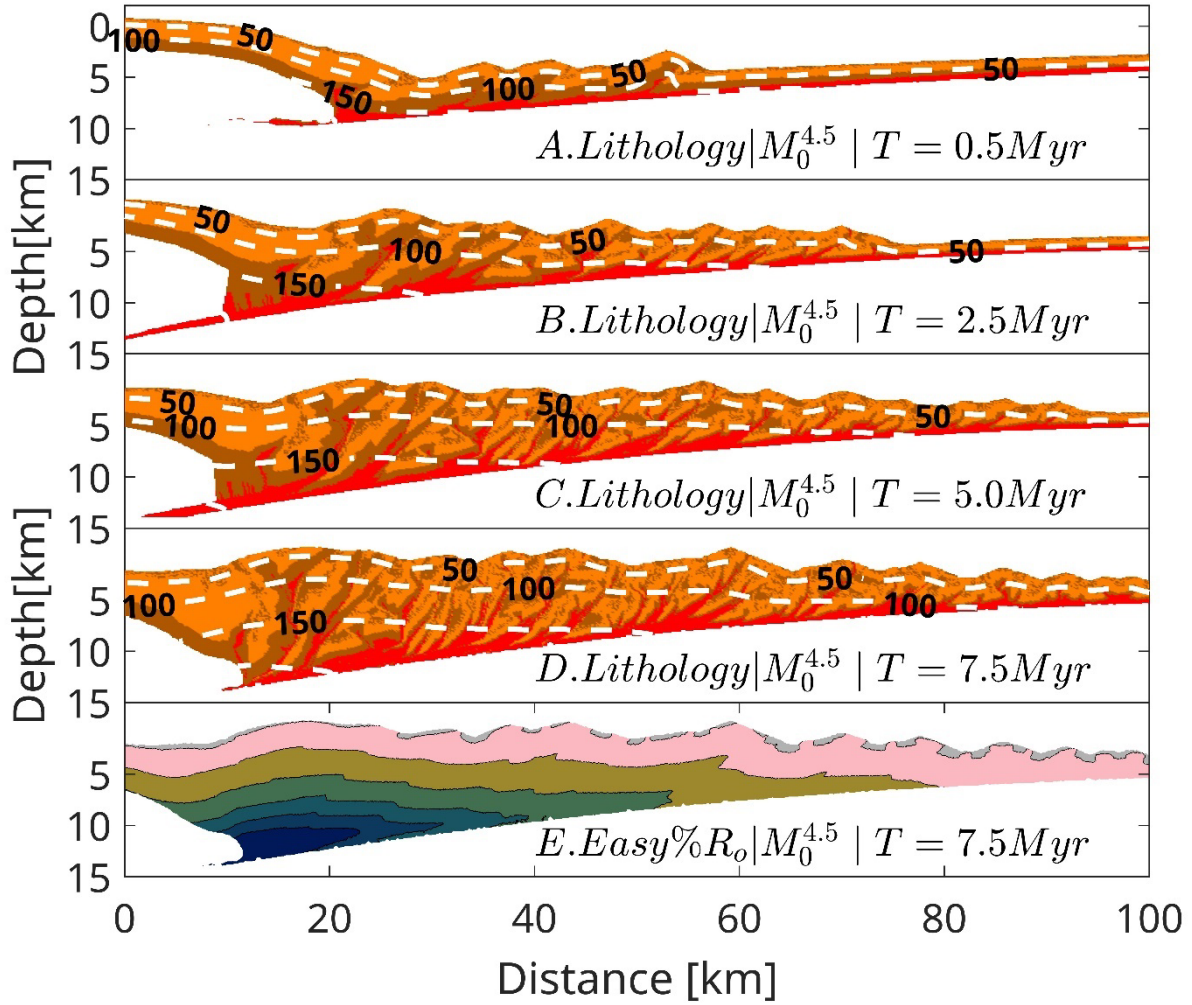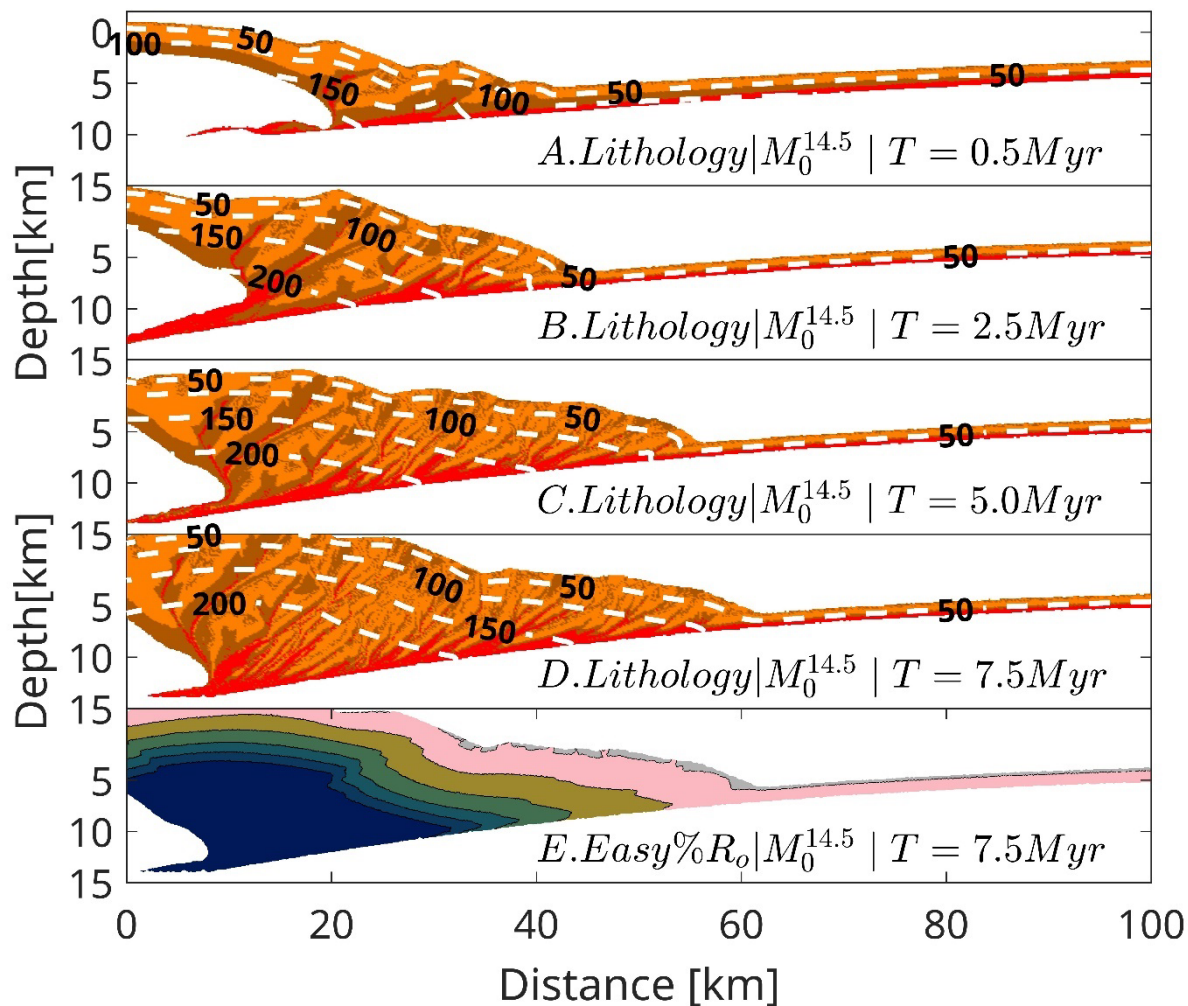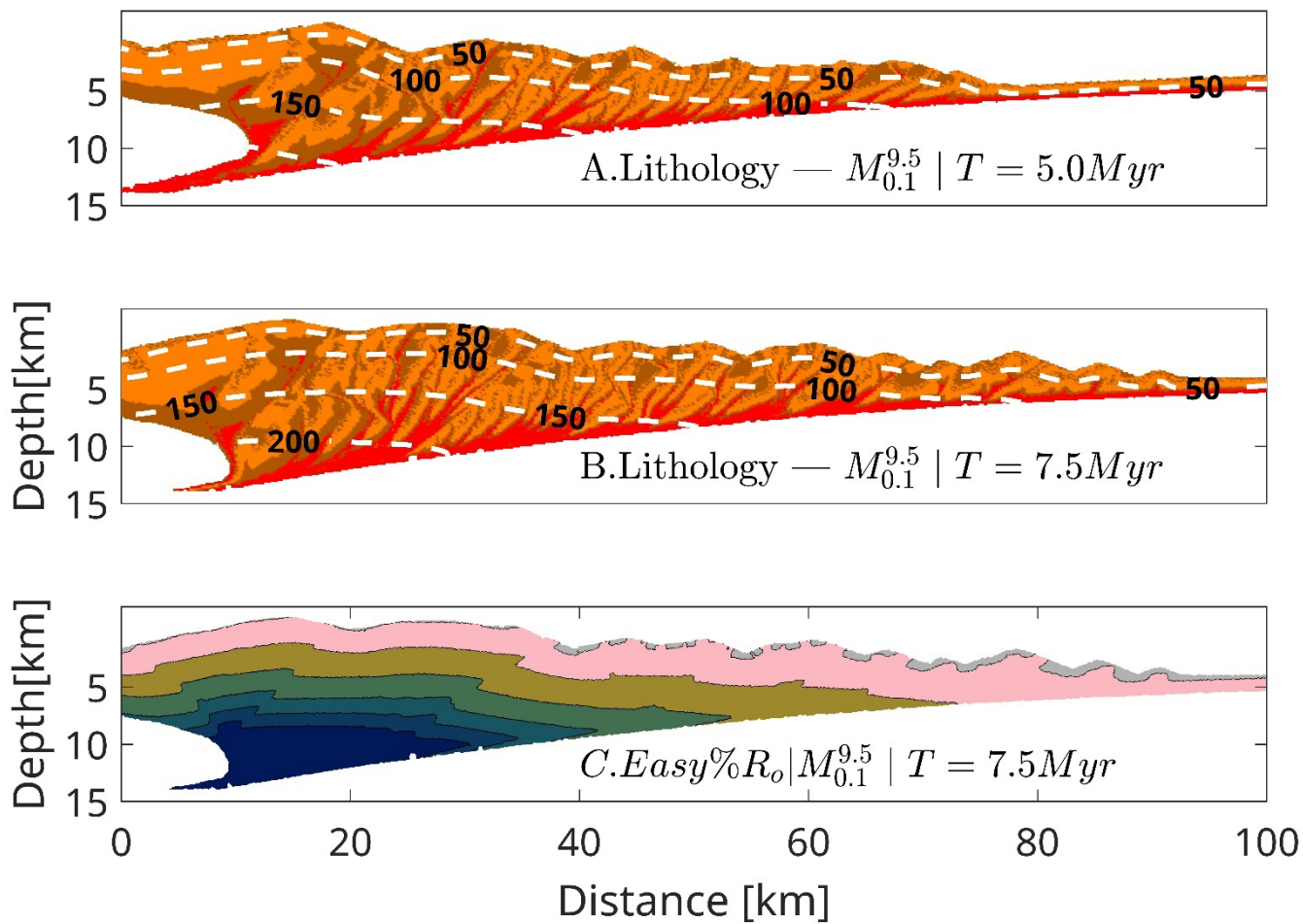
1007 ***Fig. S5:***
1008 *Typical thermomechanical evolution of the accretionary wedge for model M_0^7 at 0.5 Myr, 2.5 Myr, 5.0 Myr and 7.5 Myr of*
1009 *lithological evolution (Panel A-D). The dashed white lines represent the contours of the temperature field. The colormap for*
1010 *the first 4 panels is same as Figure 1. The last panel represents thermal maturity values at ~7.5 Myr computed using Easy%R$_o$.*
1011 *The colormap for Panel E is same as that of Figure 3.*
1012
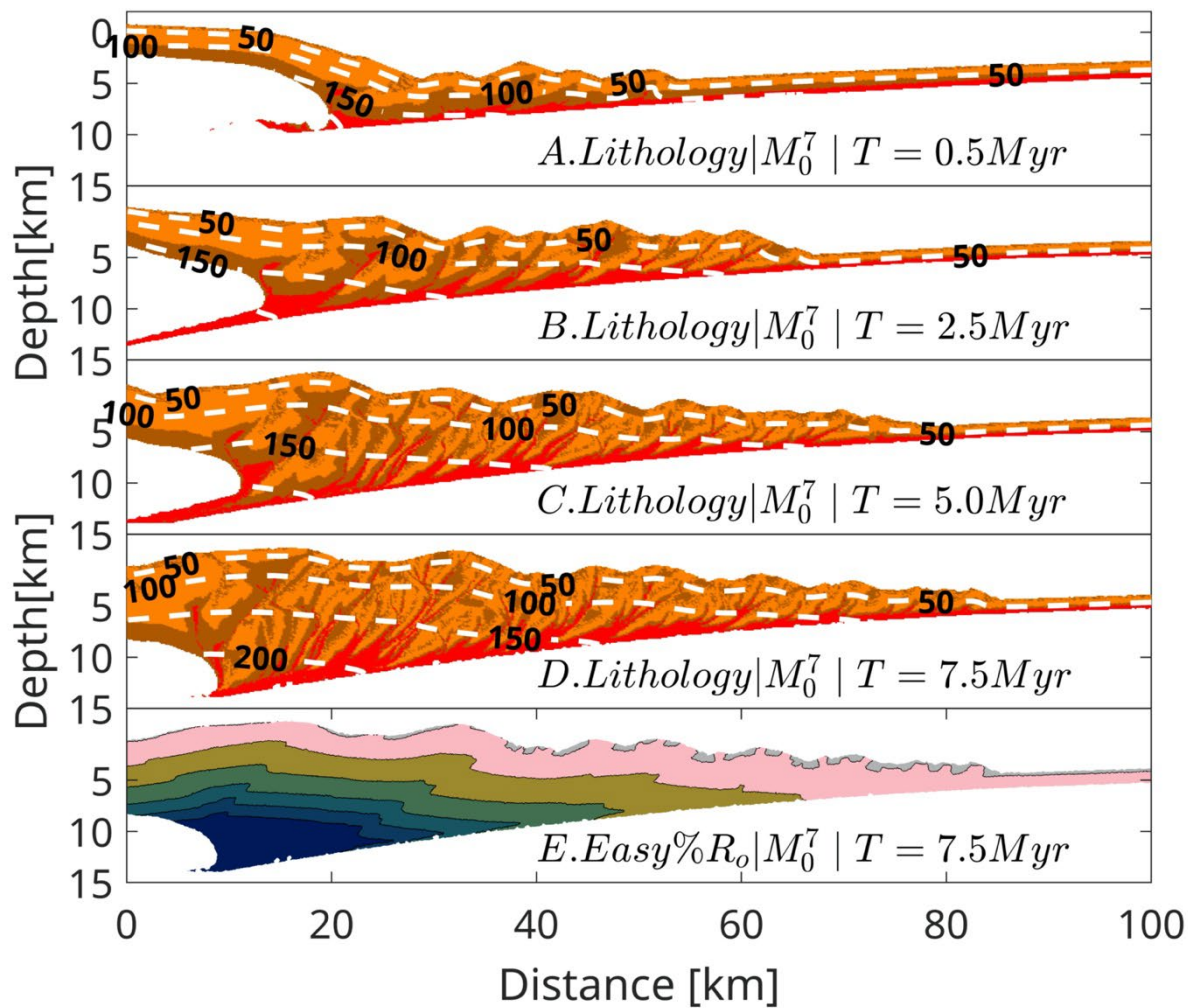
1013
1014
1015
1016
1017
1018

Fig. S6:

1020 *Typical thermomechanical evolution of the accretionary wedge for model $\mathbf{M_0^{9.5}}$ at 0.5 Myr, 2.5 Myr, 5.0 Myr and 7.5 Myr of*
1021 *lithological evolution (Panel A-D). The dashed white lines represent the contours of the temperature field. The colormap for*
1022 *the first 4 panels is same as Figure 1. The last panel represents thermal maturity values at ~7.5 Myr computed using Easy%R_o.*
1023 *The colormap for Panel E is same as that of Figure 3.*
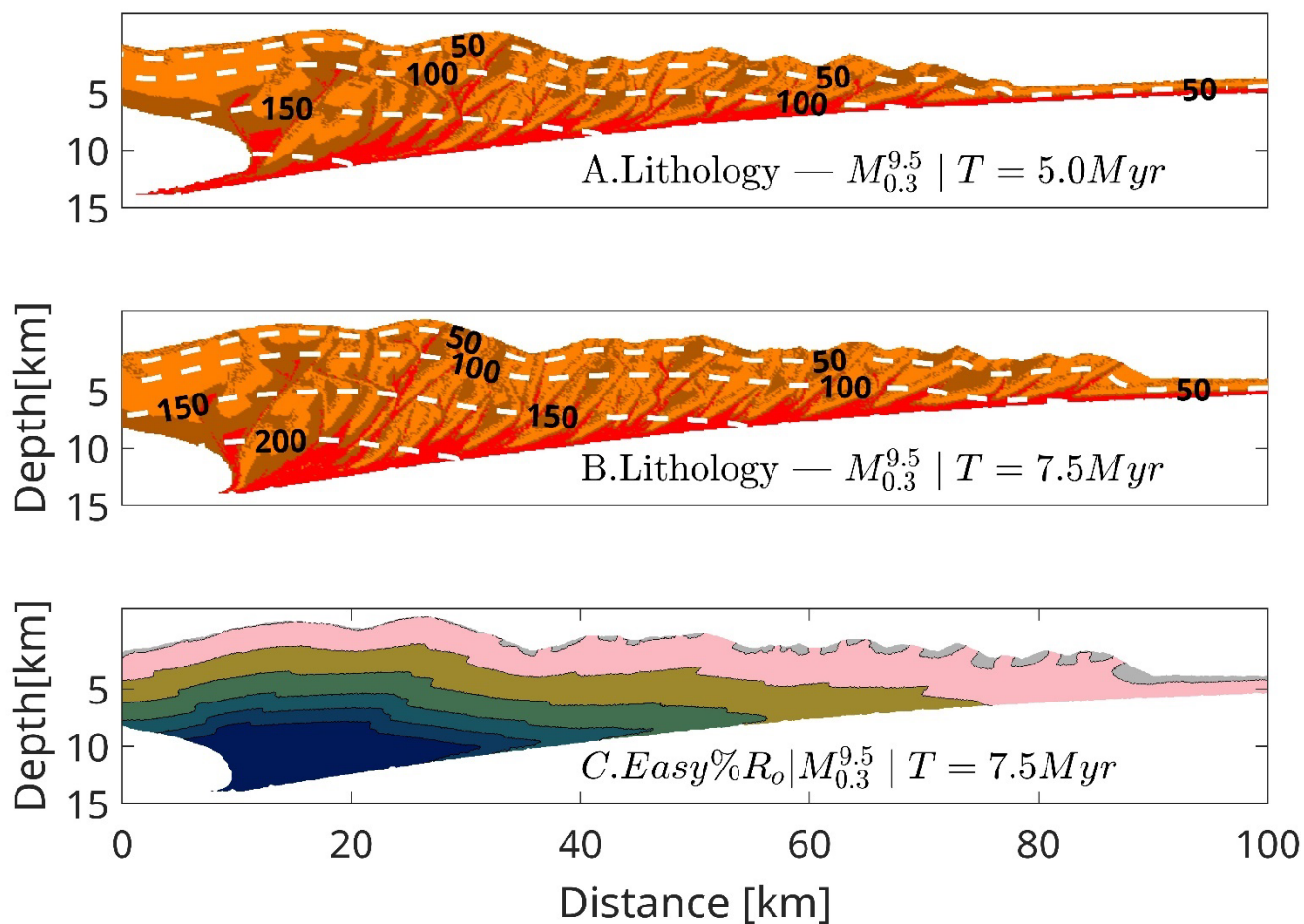
1024

1025
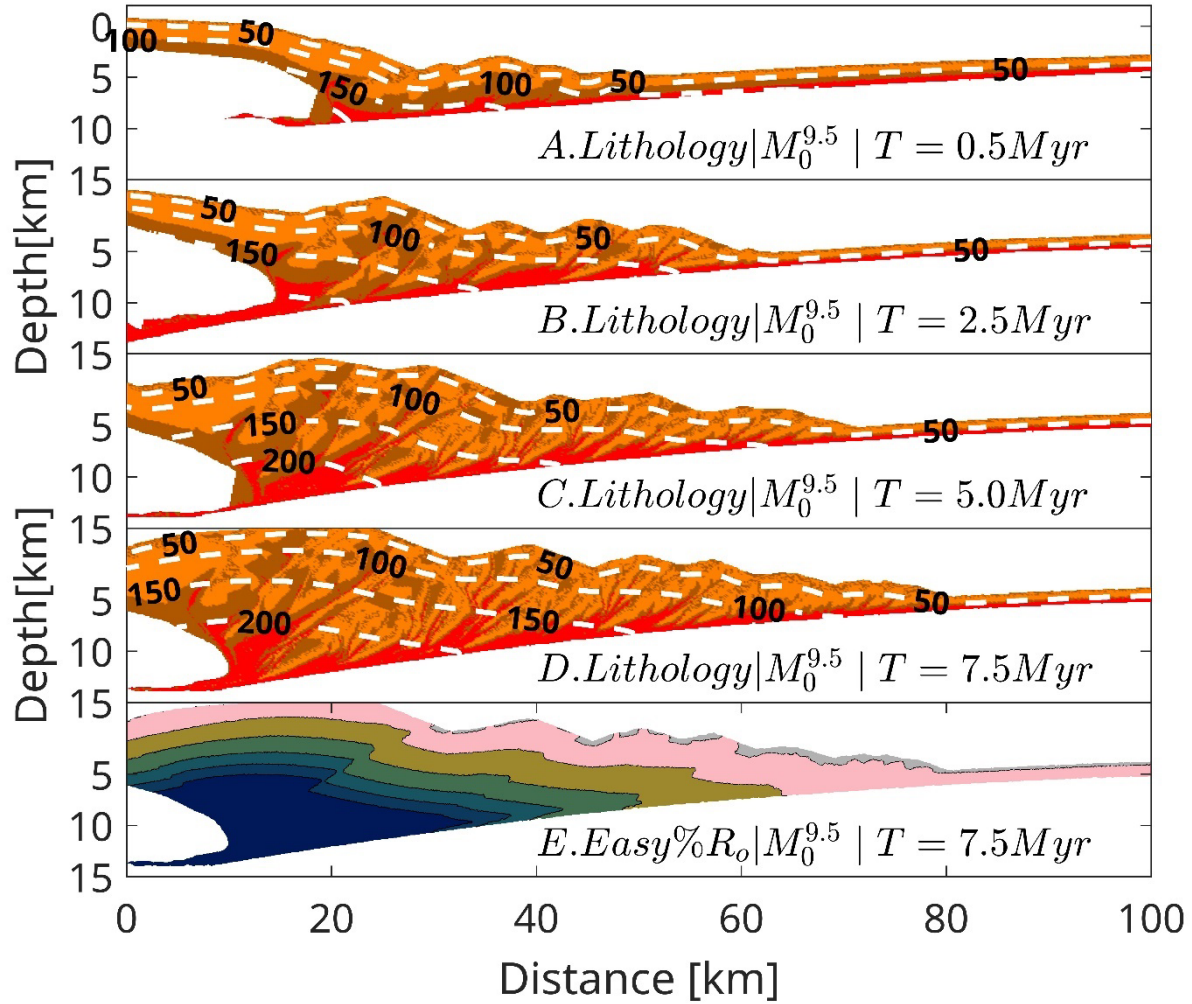
1026

1027

1028

1029

1030

1031

1033 *Typical thermomechanical evolution of the accretionary wedge for model M_0^{12} at 0.5 Myr, 2.5 Myr, 5.0 Myr and 7.5 Myr of*
1034 *lithological evolution (Panel A-D). The dashed white lines represent the contours of the temperature field. The colormap for*
1035 *the first 4 panels is same as Figure 1. The last panel represents thermal maturity values at ~7.5 Myr computed using Easy%R_o.*
1036 *The colormap for Panel E is same as that of Figure 3.*
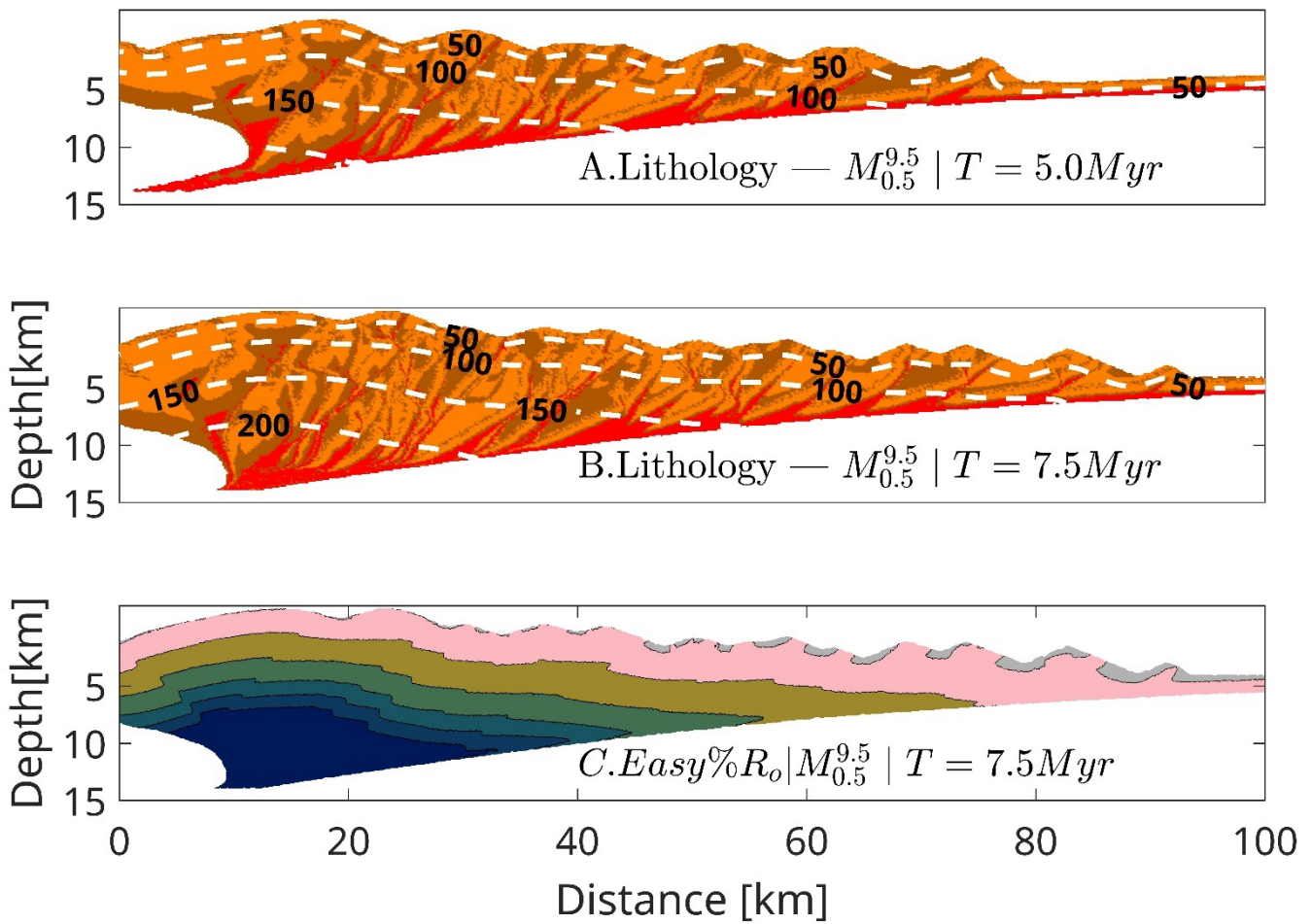
1037

1038
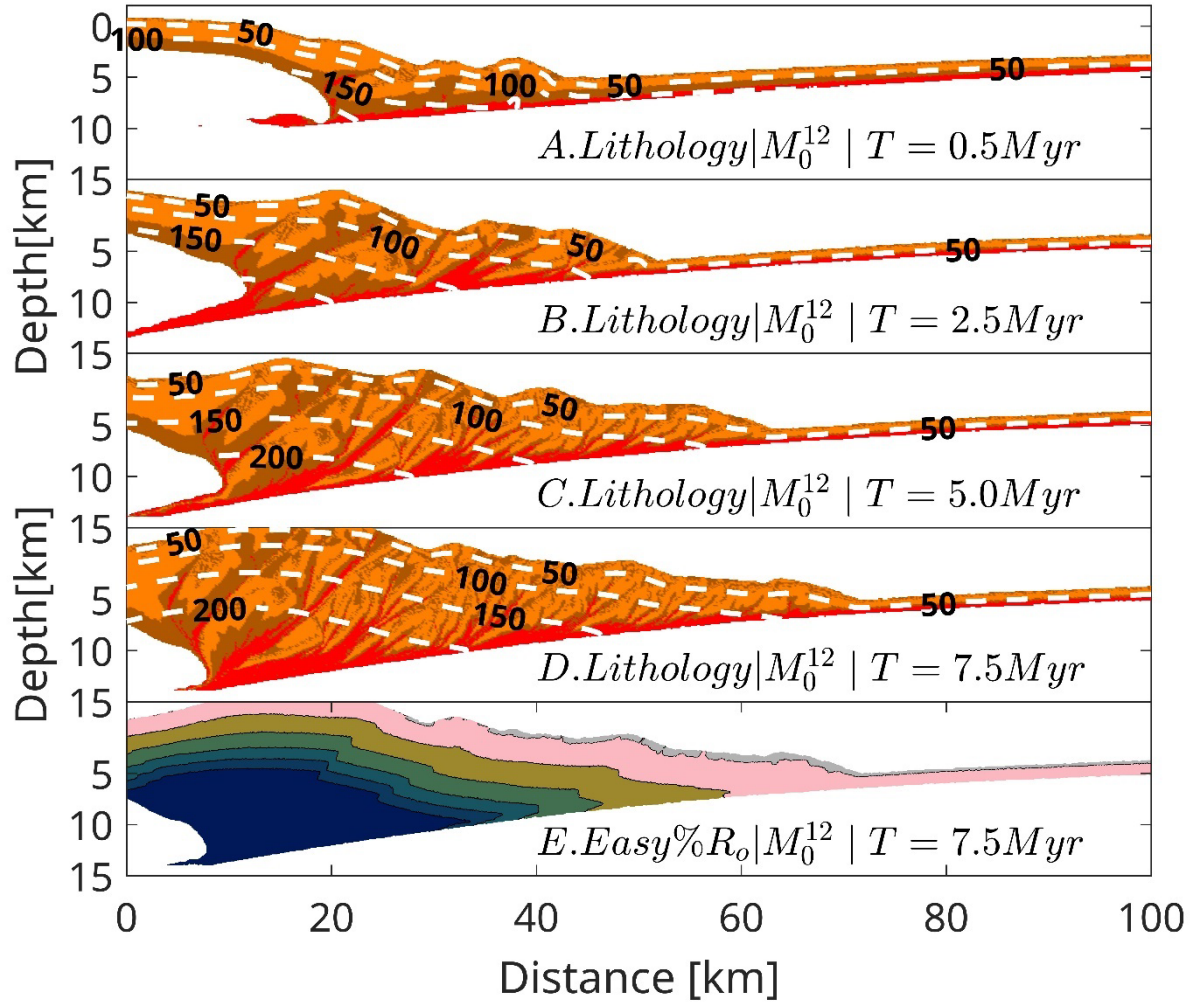
1039

1040

1041

1042

1043

Fig. S8:

Typical thermomechanical evolution of the accretionary wedge for model $M_0^{14.5}$ at 0.5 Myr, 2.5 Myr, 5.0 Myr and 7.5 Myr of lithological evolution (Panel A-D). The dashed white lines represent the contours of the temperature field. The colormap for the first 4 panels is same as Figure 1. The last panel represents thermal maturity values at ~7.5 Myr computed using Easy%R$_o$. The colormap for Panel E is same as that of Figure 3.

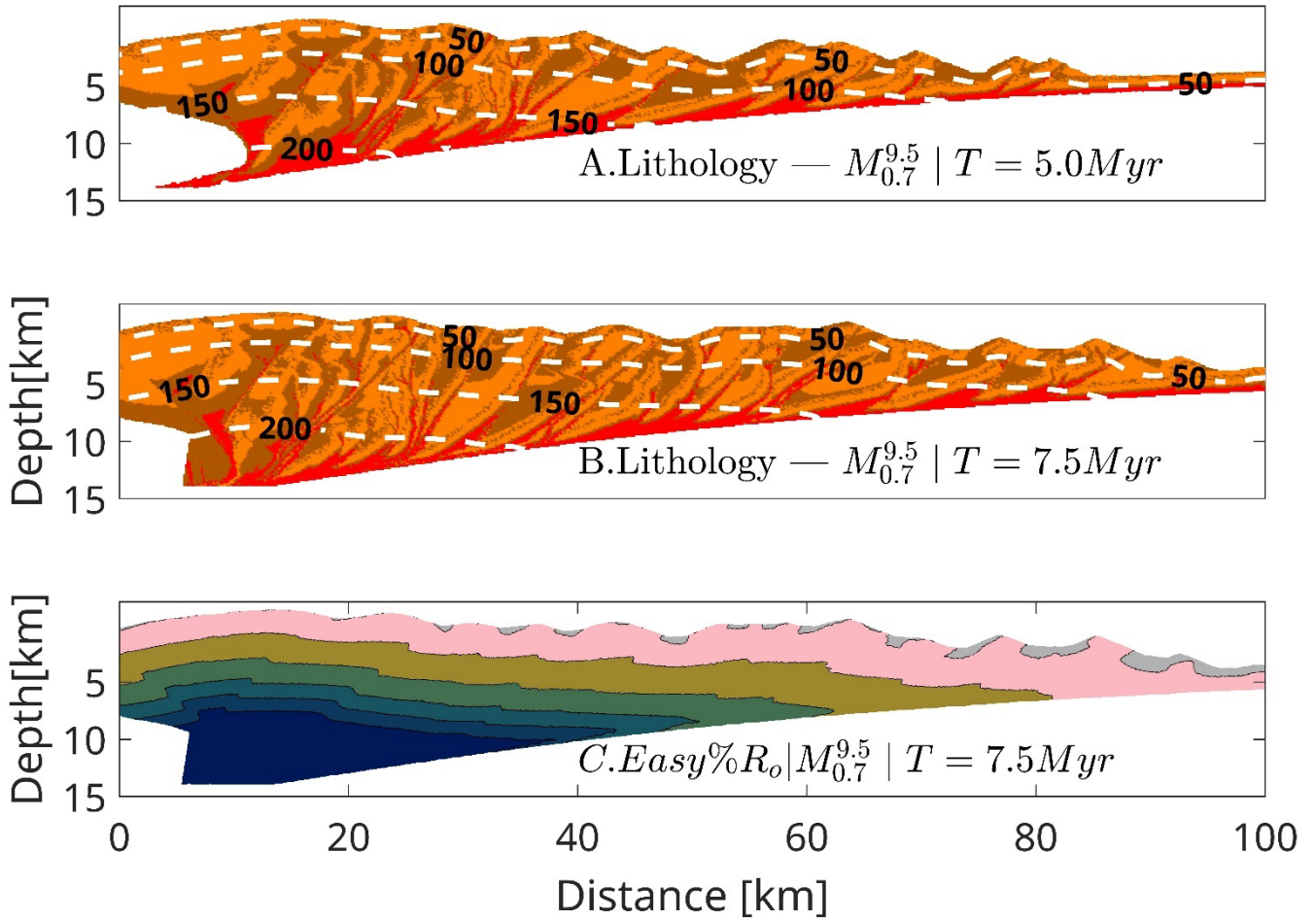1056 *Typical thermomechanical evolution of the accretionary wedge for model $M_{0.1}^{9.5}$ at 5.0 Myr and 7.5 Myr of lithological evolution*
1057 *(Panel A-B). The dashed white lines represent the contours of the temperature field. The colormap for the first 2 panels is*
1058 *same as Figure 1. The Panel C represents thermal maturity values at ~7.5 Myr computed using Easy%R_o. The colormap for*
1059 *Panel E is same as that of Figure 3.*

1060

1061

1062

1063

1064

1065

1066

1067

Fig. S10:

Typical thermomechanical evolution of the accretionary wedge for model $M_{0.3}^{9.5}$ at 5.0 Myr and 7.5 Myr of lithological evolution (Panel A-B). The dashed white lines represent the contours of the temperature field. The colormap for the first 2 panels is same as Figure 1. The Panel C represents thermal maturity values at ~7.5 Myr computed using Easy%R$_o$. The colormap for Panel E is same as that of Figure 3.

1081

1082 ***Fig. S11:***
1083 *Typical thermomechanical evolution of the accretionary wedge for model $M_{0.5}^{4.5}$ at 5.0 Myr and 7.5 Myr of lithological evolution*
1084 *(Panel A-B). The dashed white lines represent the contours of the temperature field. The colormap for the first 2 panels is*
1085 *same as Figure 1. The Panel C represents thermal maturity values at ~7.5 Myr computed using Easy%R$_o$. The colormap for*
1086 *Panel E is same as that of Figure 3.*

1087

1088

1089
1090
1091
1092
1093

1094 ***Fig. S12:***
1095 *Typical thermomechanical evolution of the accretionary wedge for model $M_{0.7}^{9.5}$ at 5.0 Myr and 7.5 Myr of lithological evolution*
1096 *(Panel A-B). The dashed white lines represent the contours of the temperature field. The colormap for the first 2 panels is*
1097 *same as Figure 1. The Panel C represents thermal maturity values at ~7.5 Myr computed using Easy%R$_o$. The colormap for*
1098 *Panel E is same as that of Figure 3.*
1099

1100

1107

1108 **_Fig. S13:_**

1109 _Typical thermomechanical evolution of the accretionary wedge for model $M_{0.9}^{9.5}$ at 5.0 Myr and 7.5 Myr of lithological evolution_
1110 _(Panel A-B). The dashed white lines represent the contours of the temperature field. The colormap for the first 2 panels is_
1111 _same as Figure 1. The Panel C represents thermal maturity values at ~7.5 Myr computed using Easy%R_o. The colormap for_
1112 _Panel E is same as that of Figure 3._

1113

1114
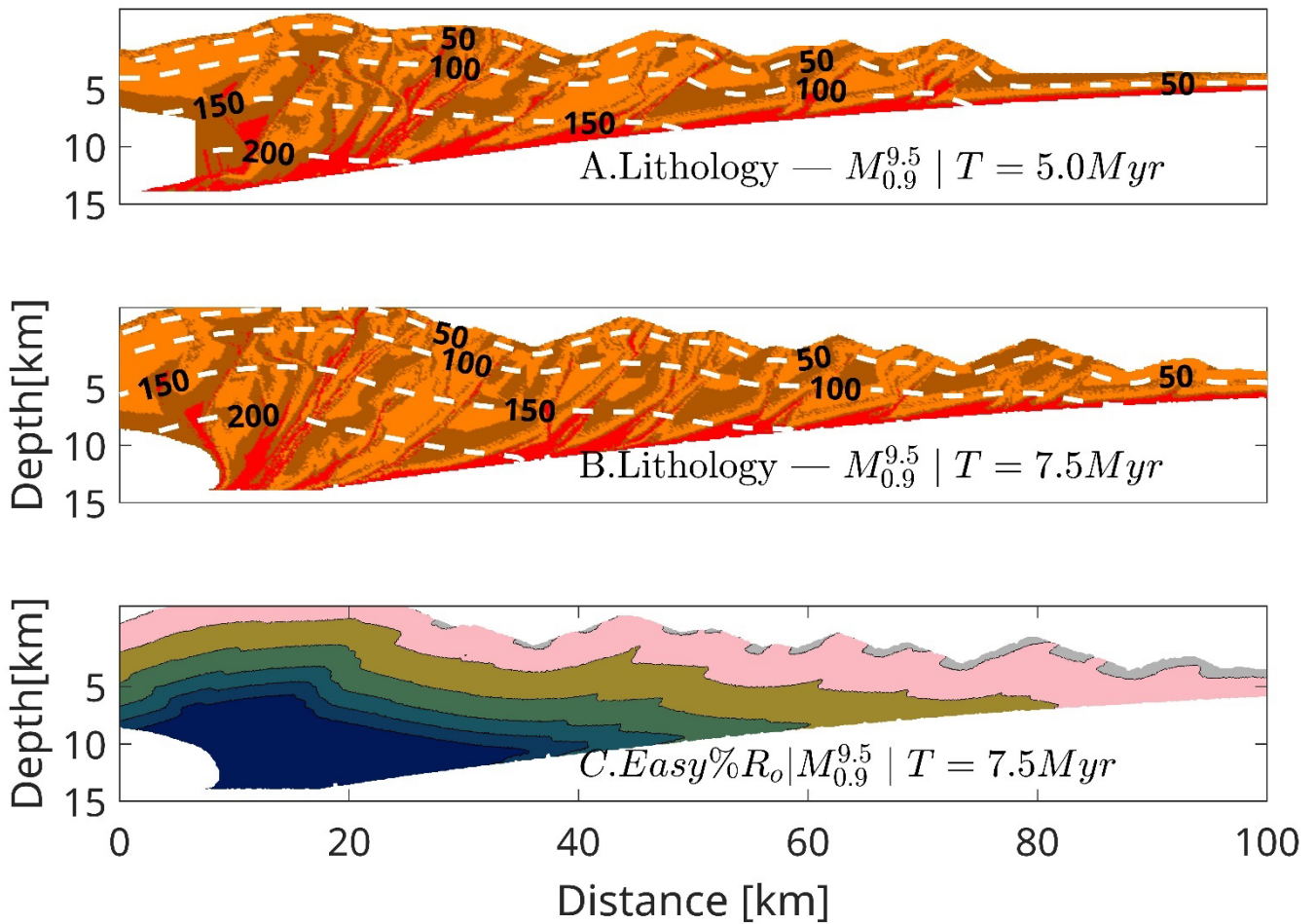
1115

1116

1117

1118

1119

1120

1121

1122

1123

1124

1125

1126

1127

1128

1129

1130

1131

1132

1133

1134

1135

1136

1137

1138

1139

1140 **Fig. S14:**
1141 *Plot of Temperature vs Depth profile in all models compared to Temperature-depth profile based on in-situ temperature from*
1142 *the long-term borehole monitoring system (indicated red patch is the range of temperature estimated by (Sugihara et al.,*
1143 *2014)). The temperature vs depth profiles for the models are computed for 20 kms from the backstop as shown in the inset.*
1144
1145
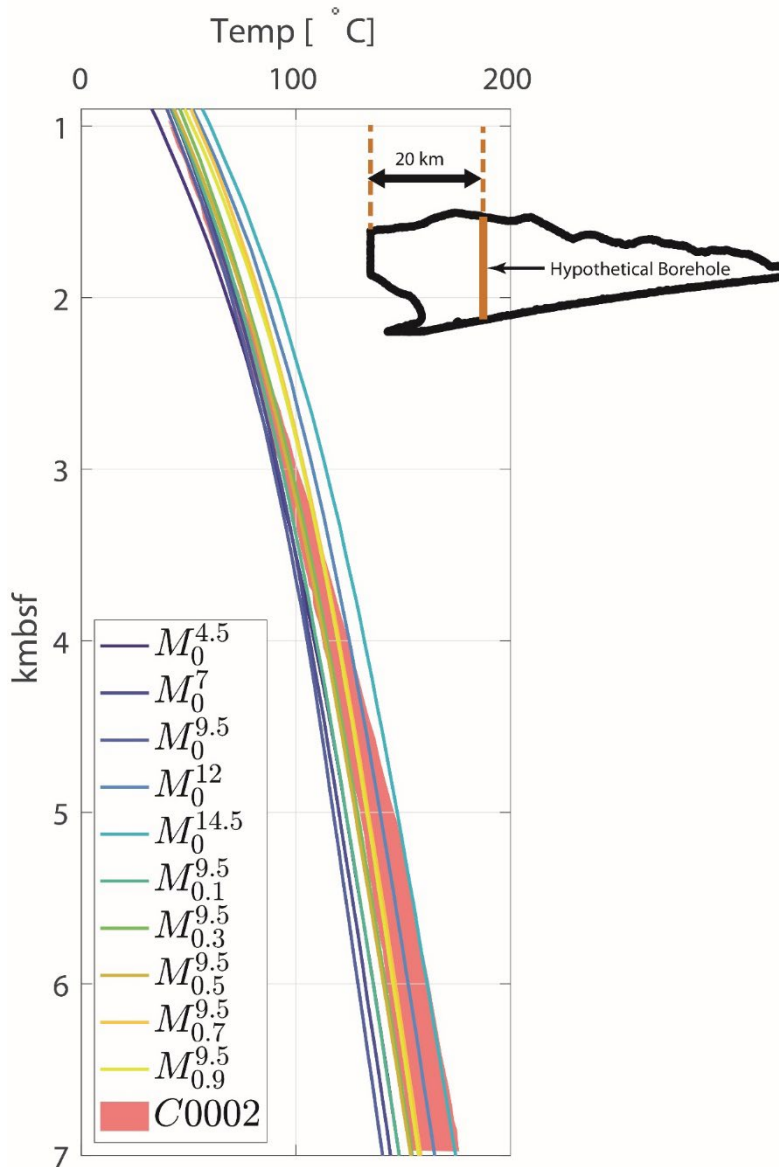
1146

Fig. S15

Trajectory of sediments in model. The wedge on top shows the location of individual boreholes relative to the position of the trench at 2.5 Myr. In each borehole, A-L 10 points are plotted for their trajectories between 2.5 Myr and 7.5 Myr. The color of markers in the trajectories represent the evolution of thermal maturity on individual sediment markers while undergoing evolution. The image of the wedge on top is a representative image showing the relative location of boreholes with respect to the trench and each other. We present 4 set of boreholes (each having 3 boreholes separated by a km), one of which lies in the wedge itself at 2.5 Myr and 3 lies in the incoming sediments as a distance of 1 km, 50km and 100 kms from trench.
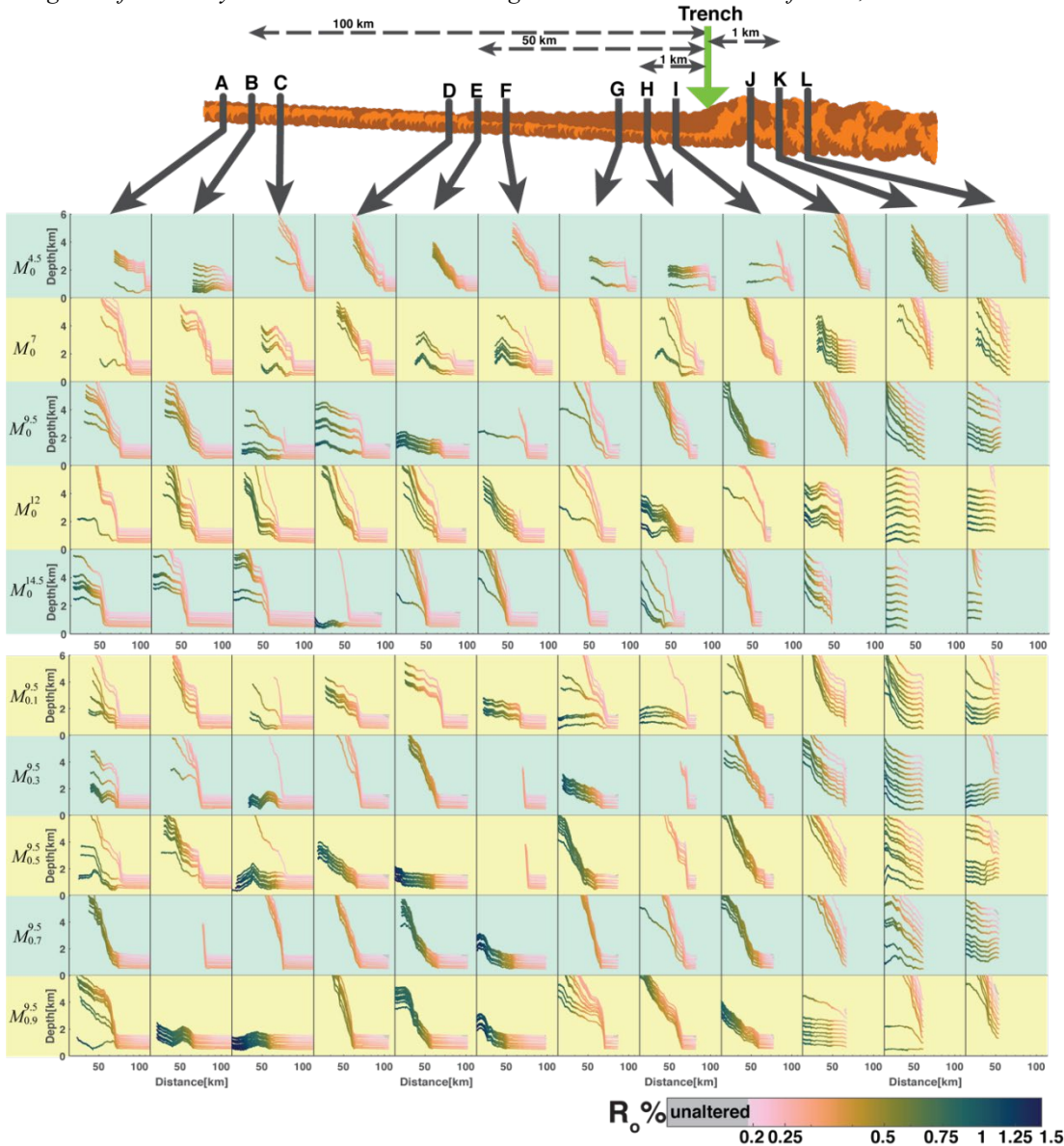
1156   **Fig. S16**

1157   *Vitrinite Reflectance(%R$_o$) vs Maximum Exposure temperature in models. Panel A, B and C show the Temperatures as a*
1158   *function of %R$_o$computed from Easy%R$_o$, Simple%R$_o$, Basin%R$_o$ for models $M_0^{4.5} - M_0^{14.5}$. Similarly panels D, E and F show*
1159   *the Temperatures as a function of %R$_o$computed from Easy%R$_o$, Simple%R$_o$, Basin%R$_o$ for models $M_{0.1}^{9.5} - M_{0.9}^{9.5}$.*

1160

1161
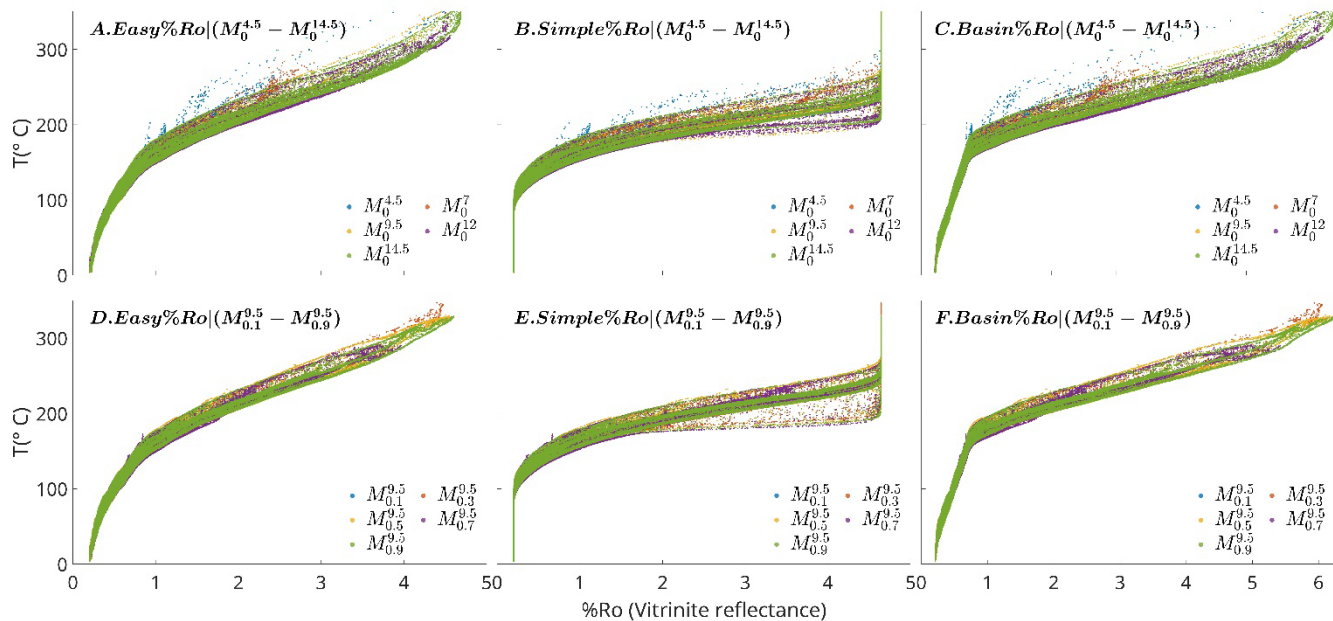
1162

1163

1164

1165

1166

1167

1168

1169

1170

1171

1172

1173

Fig. S17:

1175 *Panel A shows %R. vs T for model (shown by smaller markers) and C0002 borehole (shown by large circular markers)*
1176 *(Fukuchi et al., 2017). Y_n is the depth of the marker from the surface normalized by the thickness (vertical extent) of the wedge*
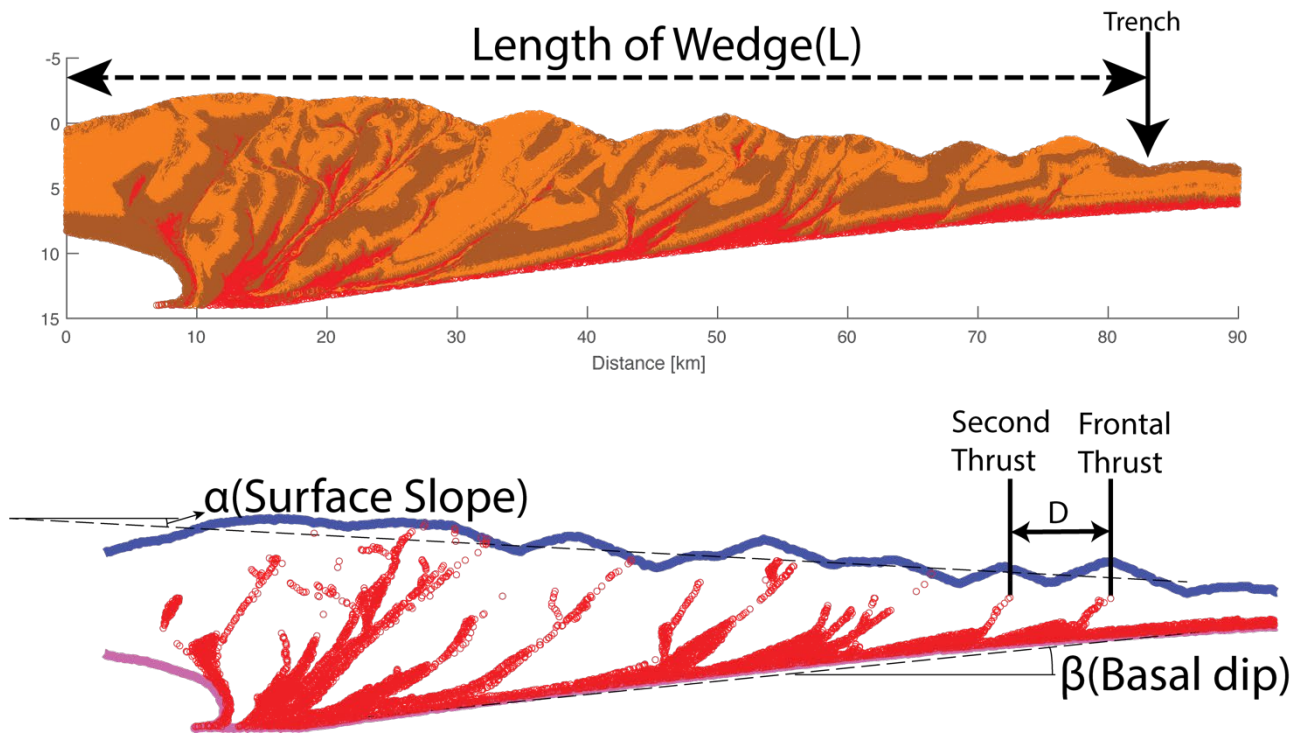1177 *at the location of the marker as illustrated in Panel B.*
1178
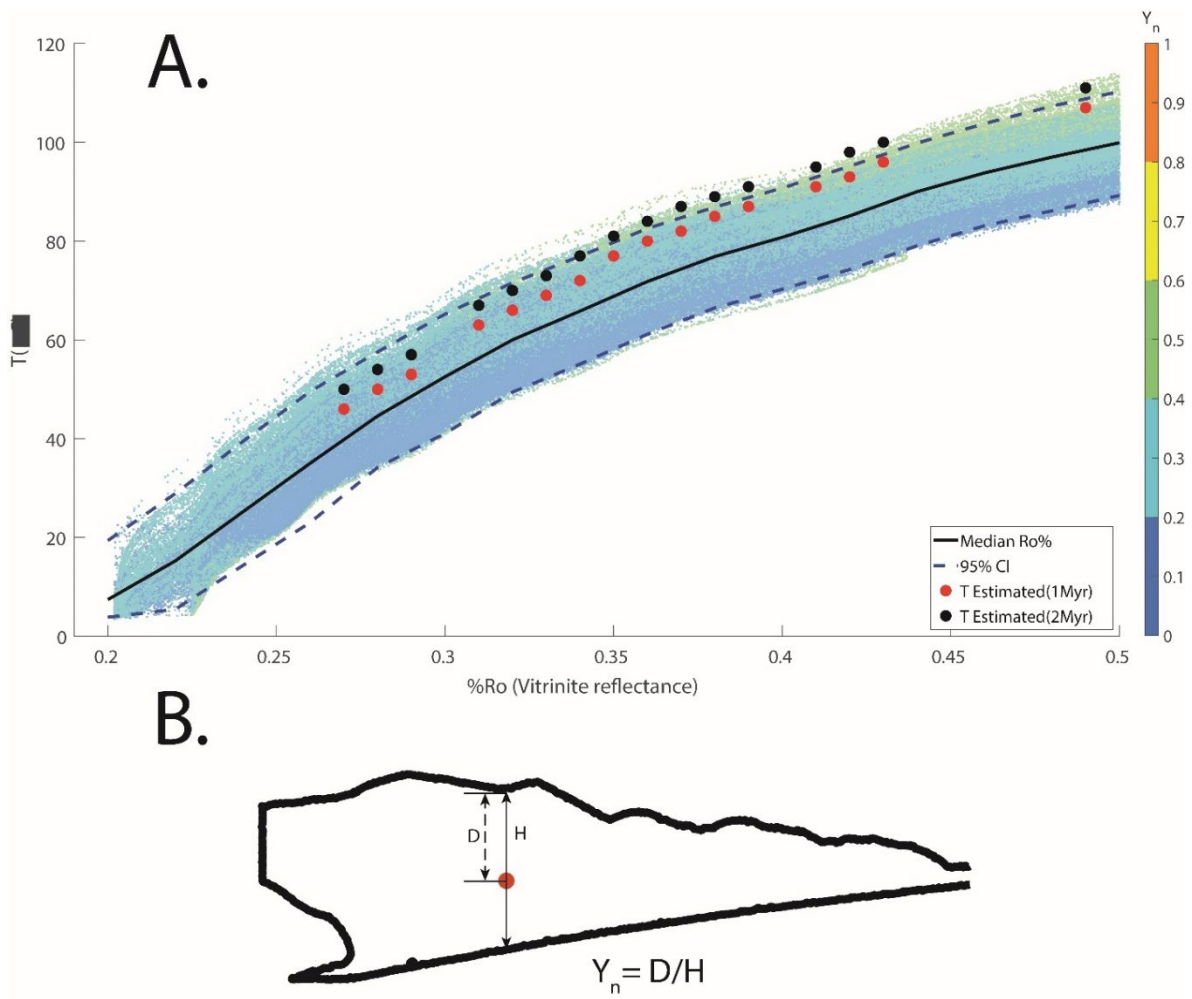
1179
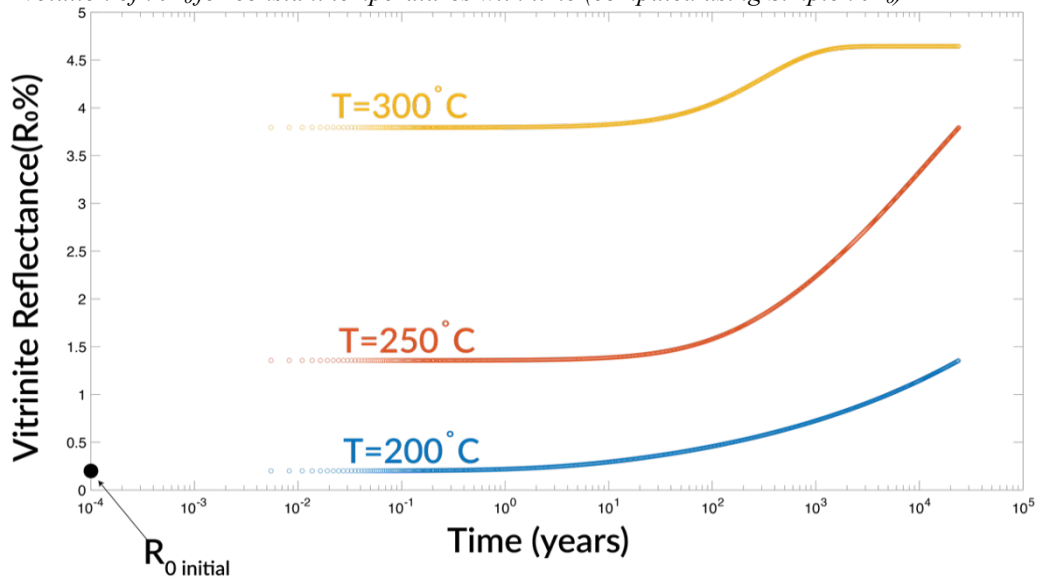
1180

1181

1182

1183

Fig. S18:

1185   Illustration to show the measurement of L (length of wedge), α (surface slope), **β**(basal dip and, D(Distance between the first
1186   and second frontal thrust).

1200   *Fig S19:*

1201   *Evolution of %R$_o$ for constant temperatures with time (computed using Simple %R$_o$)*

1202
1203   *Fig S20:*

1204   *Thermal maturity distribution in two models with different convergent velocity. Panel A and B shows a models with convergent*
1205   *velocity of 5 cm/yr and 7.5 cm/yr respectively. The colormap for the images is same as for Figure 3. The comparison between*
1206   *the models has been shown for different time to keep the volume of incoming sediments (T*V$_{conv}$) similar.*
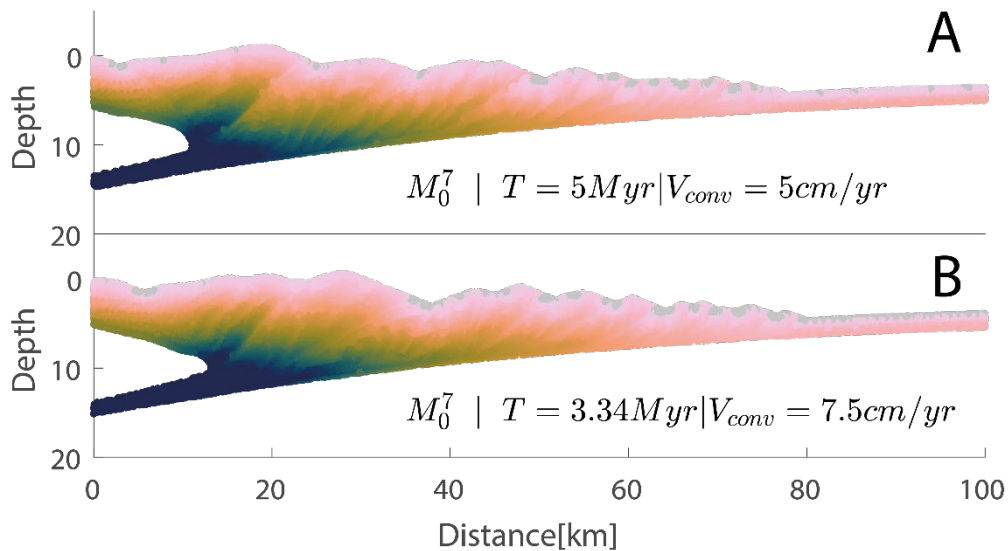
1207
1208
1209

1210
1211 *Fig S21:*

1212 *Distribution of viscosity in a representative model at 0.5 Myr, 2.5 Myr, 5.0 Myr and 7.5 Myr.*
1213